

Modeling the Shape of Axisymmetric Skyrmions in Magnetic Multilayers

William Legrand,^{1,*} Nathan Ronceray,^{1,2} Nicolas Reyren,¹ Davide Maccariello,¹ Vincent Cros,^{1,†} and Albert Fert¹

¹*Unité Mixte de Physique, CNRS, Thales, Univ. Paris-Sud, Université Paris-Saclay, Palaiseau 91767, France*

²*École Polytechnique, Palaiseau 91128, France*



(Received 5 July 2018; revised manuscript received 28 September 2018; published 18 December 2018)

We present a comprehensive micromagnetic model of isolated axisymmetric skyrmions in magnetic multilayers with perpendicular anisotropy. Most notably, the essential role of the internal dipolar field is extensively considered with a minimum amount of assumptions on the magnetization profiles. The three-dimensional structure of the multilayered skyrmions is modeled by their radial profiles in each layer. We first compare the results of the model against a full micromagnetic description in Cartesian coordinates. Our model combines information on both layer-dependent size and chirality of the skyrmions. We also provide a convenient criterion in order to characterize the stability of skyrmions against anisotropic elongations that would break their cylindrical symmetry, which allows us to confirm the stability of the determined solutions. Because this model is able to treat magnetization configurations twisted through the thickness of multilayered skyrmions, it can provide predictions on any potential hybrid chirality in skyrmions due to the interplay of Dzyaloshinskii-Moriya and dipolar interactions in multilayers. We finally apply the results of our model to the description of the current-driven dynamics of hybrid chiral skyrmions. Using the Thiele formalism, we show that we can predict the forces exerted on the multilayered skyrmions by vertical spin-polarized currents, which provides a method to conform hybrid skyrmion chiralities and spin-current injection geometries in order to optimize skyrmion motion in multilayers, to the aim of maximizing the current-induced velocity, or canceling the skyrmion Hall angle.

DOI: [10.1103/PhysRevApplied.10.064042](https://doi.org/10.1103/PhysRevApplied.10.064042)

I. INTRODUCTION

In recent years, the discovery of Dzyaloshinskii-Moriya interaction (DMI), not only driven by crystalline order [1,2], but also by interface inversion asymmetry [3,4], increased the interest for noncollinear magnetic configurations in thin magnetic films and multilayers. Beyond the ferromagnetic and antiferromagnetic configurations, the action of the DMI results in the stabilization of nonuniform configurations where the magnetic order is rotating in one or several directions of the film plane. Among these configurations, the most studied over the last couple years may probably be the magnetic skyrmions [5,6], either under the form of isolated skyrmions [7–9] or skyrmion lattices [10,11]. In a magnetic skyrmion, the magnetization vector in the structure actually maps all directions, resulting in a swirling arrangement, where the magnetization in the center of the structure (the core of the skyrmion) is the opposite of the magnetization in its surrounding environment (see Fig. 1). Moreover, due to the antisymmetric form of the DMI, a well-determined chirality (that is crucial for the spin-torque induced motion) is expected to emerge from

these skyrmion configurations, which is determined by the direction and sign of the DMI vector, resulting in a unique rotational sense for the magnetization. This fixed chirality sets a unique, topologically nontrivial configuration for the magnetic order, which results in chirality-related and topology-related effects both in the dynamics of skyrmions (efficient spin-current-induced motion [9,12], skyrmion Hall effect [13–16]) and in the transport properties of skyrmionic systems (topological Hall effect [13,17,18]). These properties are foreseen as extremely suitable for the realization of very compact shift-register memories or logic nanodevices [19], and even of more complex neuro-inspired architectures [20,21]. Such devices rely on the efficient spin-orbit torque-induced skyrmion motion that is promised by their DMI-selected chirality [12]. However, in several recent works it has been shown that the particular chirality of the skyrmions set by the DMI could be partially or completely canceled out by competing magnetic interactions, such as the dipolar interactions between magnetic moments. In such cases, skyrmions may exhibit a complex thickness-dependent chirality [22–24], which may alter the behaviors required for applications.

In epitaxially grown ultrathin, single magnetic layers hosting skyrmions, the thickness of the ferromagnetic material is usually one or a couple of atomic layers

*william.legrand@cnrs-thales.fr

†vincent.cros@cnrs-thales.fr

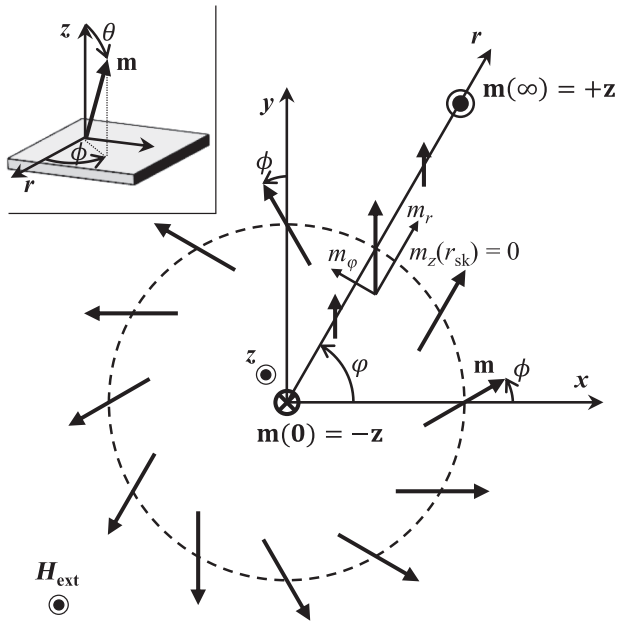


FIG. 1. Top view of the magnetization in a single ferromagnetic layer hosting a magnetic skyrmion. Thick arrows denote the reduced magnetization $\mathbf{m} = \mathbf{M}/M_S$, represented along the radial axis r and around the perimeter of the skyrmion. The axisymmetric skyrmion is fully described by its magnetization components $[m_r(r), m_\phi(r), m_z(r)]$, identical along any radial direction, where ϕ is defined as the angle between x and r directions. Here the core magnetization is $\mathbf{m}(r=0) = -\mathbf{z}$ and the surrounding magnetization is $\mathbf{m}(r=+\infty) = +\mathbf{z}$. The external field \mathbf{H}_{ext} is applied along the z direction. Inset: Definition of magnetization angles, with θ the polar angle and ϕ the azimuthal angle.

[25,26]. In these systems, the thickness of the ferromagnetic material t is then much less than the characteristic dipolar length $l_{\text{dip}} = \sigma/(\mu_0 M_S^2)$, where σ is the domain wall energy density, and M_S the saturation magnetization. For this reason, it is adequate to neglect the long-range effects of the dipolar field. The dipolar interactions are then equivalent to a reduction of the out-of-plane uniaxial magnetic anisotropy K_u to an effective magnetic anisotropy $K_{\text{eff}} = K_u - \mu_0 M_S^2/2$. In this case, the magnetization texture and the unique chirality set by the DMI remain largely unaffected by the dipolar interactions.

In slightly thicker magnetic layers [27,28], needed to stabilize skyrmions up to room temperature, the requirement of keeping a perpendicular magnetic anisotropy in spite of the mainly interfacial origin of this anisotropy limits the thickness of the ferromagnetic layer to at most 2 nm [29]. Nevertheless, such thicknesses are already large enough for the dipolar interactions to play a critical role in the stabilization of the skyrmions. As the domain wall energy density $\sigma = 4\sqrt{AK_{\text{eff}}} - \pi D$ (where A is the standard exchange stiffness, and D is the DMI magnitude) is drastically reduced in the presence of the DMI that

stabilizes the skyrmions, $t \approx l_{\text{dip}}$ and the dipolar energies are no longer negligible [28,30,31]. In all practical cases, even if skyrmion energies and sizes are significantly affected, the DMI is still strong enough to ensure a unique chirality of the skyrmions. However, in such single magnetic layers the thermal stability of the skyrmions often remains too weak, so that undesired fluctuation of the skyrmion position [32] and/or spontaneous creation or annihilation of skyrmions [14] have been observed. Room-temperature applications of magnetic skyrmions require finding solutions to improve the thermal stability of skyrmionic bits, which we believe can be achieved using the numerical modeling described in this work.

A very efficient approach in order to enhance the room-temperature stability of magnetic skyrmions is to stack several ferromagnetic layers by repeating an asymmetric combination of three or four layers, including also heavy-metal layers and spacers in contact with the ferromagnetic layers [8,9,16,33,34]. In this way, the effective magnetic volume of the skyrmions is increased, without affecting the DMI and the perpendicular magnetic anisotropy in each single layer, which allows skyrmions to better resist thermal fluctuations. Such skyrmions in multilayered systems may be called columnar skyrmions, as they are actually made of a vertically aligned stacking of coupled skyrmions hosted by each individual ferromagnetic layer. In many-repeat multilayers or for large saturation magnetization M_S values, a very good thermal stability can be achieved even at room temperature. However, the counterpart is that the dipolar field becomes very significant in these systems, not only modifying the energies of the skyrmions but also affecting their internal magnetization texture [35,36]. The demagnetizing effects of the dipolar field are predicted to cause a rotation of the in-plane magnetic moments of the skyrmions, driving a reorientation from Néel skyrmions, as favored by the form of the interfacial DMI, into Bloch skyrmions, as favored by the dipolar interactions. As the efficiency of the spin-orbit torque-driven motion of skyrmions in multilayered nanotracks originates in their Néel configuration [12], a right balance is required between enough layers to reach sufficient thermal stability, but few enough layers to mitigate the reorientation effect of dipolar interactions [36].

Beyond such a Néel-to-Bloch transition effect, we have demonstrated experimentally in a previous work [24] that despite the presence of a large DMI in Pt/Co/AlO_x based magnetic multilayers, the in-plane magnetic moments of the skyrmions are actually reversed by the dipolar interactions in some, but not all, of the magnetic layers, resulting in the stabilization of hybrid chiral structures. It is thus to be emphasized that above a critical number of repetitions of the magnetic layers, the chirality of the skyrmions thus varies across the thickness of the multilayers [24] instead of reorienting coherently through the layers. The magnetization texture is thus no longer

z independent, contrary to what has been often hypothesized. Because the current-driven dynamics of skyrmions are related to the details of their internal magnetization texture [12], such alterations of the chirality are important and require particular attention, in order to understand how to efficiently manipulate such skyrmions with currents [9,16,19,37]. However, to date, most attempts in order to model the profile of magnetic skyrmions consider a uniform magnetization across the thickness of the stack and have neglected the layer-by-layer variations of the magnetic configuration.

It is the central objective of this paper to tackle these issues, by providing a numerical model that is able to predict the actual three-dimensional equilibrium profiles of axisymmetric skyrmions in magnetic multilayers. Our motivation is to take advantage of the axial symmetry of the skyrmions for in-plane-isotropic multilayers, in order to get a simple and fast determination of the solution of the energy minimization problem by reducing a tridimensional problem into a bidimensional one. This technique has already been applied to the study of magnetic bubbles in thick ferromagnets [38,39]. Here, we extend this approach by including the DMI, the presence of chiral spin textures and the fact that we consider magnetic multilayers. Despite the computational complexity of quantitatively determining the dipolar field without further simplifying assumptions, we find that by making use of their cylindrical symmetry the equilibrium profile of multilayered skyrmions can be determined in a reasonable time on conventional personal computers. We first validate our model by comparing the obtained profiles with reference solutions provided by the usual and multipurpose micromagnetic solver Mumax³, which uses Cartesian, tridimensional coordinates. Our method provides us with a convenient tool that we apply, as an example, to the problem of the determination of the size of skyrmions as a function of applied field and number of layers. We also introduce a similar model for double domain walls, in Cartesian coordinates, in order to quantify the stability of the skyrmion solutions against anisotropic deformations. We then rely on the main advantage of the present model, being able to determine the layer-by-layer chirality of the skyrmions, to analyze hybrid chirality in multilayered skyrmions. In turn, this allows us to predict the current-induced dynamics of these skyrmions from their equilibrium configuration, by determining the different terms of the Thiele equation. We finally provide strategies to improve the skyrmion velocity and control their direction of motion.

II. DESCRIPTION OF THE MODEL

The model that we aim to develop here is fully numerical. It differs from several recently published analytical models [36,40], in which a usual trial function is assumed to reproduce the profile of magnetic skyrmions,

parametrizing them with only a couple of parameters. Here, no other assumption will be made on the skyrmion profiles except their axial symmetry. For a given set of magnetic parameters, the present model is able to provide the minimum energy magnetization profile, directly relaxed from an arbitrary initial profile, in the limit of a very high damping. As a consequence, within our approach, any (isotropic) additional interaction can be added in the energy functional that we describe below, e.g., interlayer coupling, second-order anisotropy, etc. In contrast, in such cases the suitable trial functions may be very different and would affect the validity of analytical models. Therefore, the interest of the present model is that despite involving more computation, it allows for much more generality in the types of systems that can be described, including notably hybrid chiral skyrmions.

A. Magnetic energy terms

In ferromagnetic thin films, five interaction terms are usually considered in the energy of the magnetic configurations: Heisenberg exchange, Dzyaloshinskii-Moriya interaction, magnetic anisotropy, Zeeman interaction, and long-range dipolar interactions. In the following, to simplify the discussions we only consider a DMI vector favoring Néel walls or Néel skyrmions (DMI vector \mathbf{D} in the plane of the films and perpendicular to the vector joining the related magnetic moments), as it is most often found in metallic multilayers. Note, however, that our model can easily be adapted to other DMI vectors, adjusting the corresponding term in the following Eq. (1). For example in B20 materials, both bulk chiral interactions and dipolar interactions favor Bloch-type skyrmions inside the layers, with different surface DMI vectors [5,10]. In isotropic materials for which the DMI only has an interfacial origin, the stabilized skyrmions are axisymmetric and their energy in a ferromagnetic layer can be written as [41]

$$E_{\text{sk}} = 2\pi t \int_{r=0}^{\infty} \left\{ A (\nabla \mathbf{m})^2 + D (m_z \operatorname{div} \mathbf{m} - \mathbf{m} \nabla m_z) + K_u (1 - m_z^2) + \mu_0 H_{\text{ext}} M_S (1 - m_z) - \mu_0 M_S / 2 (M_S + \mathbf{H}_{\text{dip}} \cdot \mathbf{m}) \right\} r dr, \quad (1)$$

where t is the thickness of a single ferromagnetic layer of magnetization M_S , r is the radial distance from the center of the skyrmion, A is the exchange stiffness parameter, D is the DMI parameter, K_u is the out-of-plane uniaxial anisotropy parameter, H_{ext} is the external field (here applied perpendicular to the plane), and \mathbf{H}_{dip} is the dipolar field generated by the magnetization distribution. For thin magnetic layers, say, $t < l_{\text{dip}}$, we can consider that the magnetization does not vary along z inside a given layer. We take into account the three components of the magnetization profile at any r : $m_r(r)$ (along the radial

direction), $m_\varphi(r)$ (perpendicular to the radial direction) and $m_z(r)$ (perpendicular to the plane of the layer), as represented in Fig. 1. By introducing the dimensionless radius $\rho = r/\sqrt{A/K_{\text{eff}}}$, we get a dimensionless energy integral [42]

$$E_{\text{sk}} = 2\pi tA \int_{\rho=0}^{\infty} \left\{ \left(\frac{dm_r}{d\rho} \right)^2 + \left(\frac{dm_\varphi}{d\rho} \right)^2 + \left(\frac{dm_z}{d\rho} \right)^2 + \frac{1-m_z^2}{\rho^2} + \frac{4D}{\pi D_c} \left(\frac{m_r m_z}{\rho} + m_z \frac{dm_r}{d\rho} - m_r \frac{dm_z}{d\rho} \right) + \frac{K_u}{K_{\text{eff}}} (1-m_z^2) + \frac{\mu_0 H_{\text{ext}} M_S}{K_{\text{eff}}} (1-m_z) - \frac{\mu_0 M_S^2}{2K_{\text{eff}}} \left(1 + \frac{\mathbf{H}_{\text{dip}}}{M_S} \cdot \mathbf{m} \right) \right\} \rho d\rho, \quad (2)$$

where we introduce the critical DMI value for the onset of spin spirals at zero field [43] $D_c = 4\sqrt{AK_{\text{eff}}}/\pi$. The total energy E_{tot} is the sum of E_{sk} in all layers.

As we describe below, the effective fields $\mathbf{H}_{\text{eff}} = (H_r, H_\varphi, H_z)$ associated to each energy term can also be expressed from $\mathbf{m}(r)$. Therefore, we decide to find the equilibrium configuration $\mathbf{m}(r)$ that minimizes E_{tot} by the quasistatic time evolution of the magnetic texture under these fields as obtained from the Landau-Lifshitz equation. To this effect, we only consider the damping term and not the precession term of the Landau-Lifshitz equation (case of a very large damping). After initializing the system with a given configuration $\mathbf{m}(r)$, the system relaxes directly to the closest state of minimum energy, following the direction given by the sum of all effective fields. To perform such a minimization, at each iteration, we thus determine the step increment $\delta_{\mathbf{m}}$ representing the evolution of \mathbf{m} , obtained from the Landau-Lifshitz equation as

$$\delta_{\mathbf{m}} = -\lambda \mathbf{m} \times (\mathbf{m} \times \mathbf{H}_{\text{eff}}) = \lambda \begin{bmatrix} H_r (1-m_r^2) - H_\varphi m_r m_\varphi - H_z m_r m_z \\ H_\varphi (1-m_\varphi^2) - H_z m_\varphi m_z - H_r m_\varphi m_r \\ H_z (1-m_z^2) - H_r m_z m_r - H_\varphi m_z m_\varphi \end{bmatrix} \quad (3)$$

where λ is a constant small enough to ensure convergence. By adding successively the step increments $\delta_{\mathbf{m}}$ to \mathbf{m} , the magnetic configuration converges to the closest minimum of energy and thus minimizes E_{tot} .

The effective field \mathbf{H}_{eff} is the sum of the five field terms deriving from each energy term. The exchange field is

obtained by

$$\mathbf{H}_A = \frac{2A}{\mu_0 M_S} \nabla^2 \mathbf{m} = \frac{2A}{\mu_0 M_S} \begin{bmatrix} \frac{d^2 m_r}{dr^2} + \frac{1}{r} \frac{dm_r}{dr} - \frac{m_r}{r^2} \\ \frac{d^2 m_\varphi}{dr^2} + \frac{1}{r} \frac{dm_\varphi}{dr} - \frac{m_\varphi}{r^2} \\ \frac{d^2 m_z}{dr^2} + \frac{1}{r} \frac{dm_z}{dr} \end{bmatrix}, \quad (4)$$

the DMI field is obtained by

$$\mathbf{H}_D = \frac{2D}{\mu_0 M_S} [(\text{div} \mathbf{m}) \mathbf{z} - \nabla m_z] = \frac{2D}{\mu_0 M_S} \left[\frac{dm_z}{dr} \mathbf{r} - \left(\frac{m_r}{r} + \frac{dm_r}{dr} \right) \mathbf{z} \right], \quad (5)$$

and anisotropy and external fields are given by $\mathbf{H}_K = 2K_u m_z / (\mu_0 M_S) \mathbf{z}$ and $H_{\text{ext}} \mathbf{z}$, respectively. These four field terms are straightforward to determine because they are functions of the local magnetization and its derivatives only. However, most of the complexity in the determination of the skyrmion profiles resides in the determination of the dipolar field \mathbf{H}_{dip} . As dipolar interactions constitute a long-range interaction, \mathbf{H}_{dip} at each point is a function of the magnetization at every point in the system. In the present model, the dipolar field is also the only term that couples the different magnetic layers. Following the approach that has been developed for the study of magnetic bubbles in thick ferromagnetic layers, we can find the solution of the magnetostatic problem relying on the cylindrical symmetry of skyrmions.

B. Solution for the dipolar field

The dipolar field \mathbf{H}_{dip} is defined as the opposite of the gradient of the magnetostatic potential ψ , which satisfies Poisson's equation and specific boundary conditions, related to volume and surface magnetic charges, respectively [38,39]:

$$\begin{aligned} \text{(i)} \quad \nabla^2 \psi &= \begin{cases} M_S \text{div } \mathbf{m}, & -t/2 \leq z \leq t/2 \\ 0, & \text{outside} \end{cases} \\ \text{(ii)} \quad \nabla \psi &\xrightarrow{z \rightarrow \pm\infty} 0 \\ \text{(iii)} \quad \psi &\text{ continuous at } z = \pm t/2 \\ \text{(iv)} \quad \frac{\partial \psi}{\partial z} \Big|_{z=\pm(t/2)^-} &\pm (-M_S \mathbf{m} \cdot \mathbf{z}) = \frac{\partial \psi}{\partial z} \Big|_{z=\pm(t/2)^+}, \end{aligned} \quad (6)$$

where the ferromagnetic layer that is the source $\mathbf{m}(r)$ of the dipolar field extends between $z = -t/2$ and $z = t/2$. In the following, we apply the principle of superposition used in magnetostatic problems and neglect the interactions between volume charges in Eq. (6)(i) [$f(r) = M_S \text{div } \mathbf{m}$]

and surface charges in Eq. (6)(iv) [$h(r) = -M_S \mathbf{m} \cdot \mathbf{z}$]. This allows us to find the potentials associated to f and h separately. We thus define ψ_f the potential associated to f with $h = 0$, and ψ_h the potential associated to h with $f = 0$.

The resolution of Poisson's equation in cylindrical symmetry uses Hankel transforms, the equivalent of Fourier transform for axisymmetric functions. We choose the Bessel function of the first kind, order 0, J_0 and thus define for any function $g(r)$ its Hankel transform

$$\bar{g}(k) = \int_{r=0}^{\infty} r J_0(kr) g(r) dr. \quad (7)$$

For the magnetic potential, which satisfies $\Delta\psi = f$ or 0, its Hankel transform $\bar{\psi}(k, z)$ then verifies for any k, z

$$\frac{\partial^2 \bar{\psi}(k, z)}{\partial z^2} - k^2 \bar{\psi}(k, z) = \bar{f} \text{ or } 0, \quad (8)$$

which allows us to find $\bar{\psi}$ by solving the partial differential equation. The detail of the resolution is given in [Appendix A](#). We get for the potentials originating from the volume charges f and the surface charges h

$$\bar{\psi}_f = \begin{cases} \frac{\bar{f}}{k^2} \exp(-kt/2) \cosh(kz) - \frac{\bar{f}}{k^2}, & 0 \leq z \leq t/2 \\ \frac{-\bar{f}}{k^2} \sinh(kt/2) \exp(-kz), & z > t/2 \end{cases}$$

$$\bar{\psi}_h = \begin{cases} \frac{-\bar{h}}{k} \exp(-kt/2) \sinh(kz), & 0 \leq z \leq t/2 \\ \frac{-\bar{h}}{k} \sinh(kt/2) \exp(-kz), & z > t/2 \end{cases} \quad (9)$$

that can be completed by symmetry. As volume charges are symmetric with respect to z while surface charges are antisymmetric, we have that

$$\bar{\psi}_f(k, z) = +\bar{\psi}_f(k, -z),$$

$$\bar{\psi}_h(k, z) = -\bar{\psi}_h(k, -z). \quad (10)$$

The fields acting on a given layer l_j at position z' (either the source layer l_i itself or another layer) along r and z are finally obtained by transforming back $\bar{\psi}_{f,h}$ into $\psi_{f,h}$ using the inverse Hankel transform, and then averaging $\partial\psi_{f,h}/\partial r$ and $\partial\psi_{f,h}/\partial z$ over the thickness t' of the affected layer l_j

$$H_{\text{dip},r}^{i,j}(r) = -\frac{1}{t'} \int_{z=z'-t'/2}^{z'+t'/2} \left(\frac{\partial\psi_f}{\partial r} + \frac{\partial\psi_h}{\partial r} \right) dz, \quad (11)$$

$$H_{\text{dip},z}^{i,j}(r) = \frac{(\psi_f + \psi_h)|_{z'-t'/2} - (\psi_f + \psi_h)|_{z'+t'/2}}{t'}.$$

Thus, $\mathbf{H}_{\text{dip}}[\mathbf{m}_i(r), t, t', \Delta z]$ is defined as a function of source magnetization configuration $\mathbf{m}_i(r)$ and layer thickness $t = t_i$, affected layer thickness $t' = t_j$, and interlayer spacing

Δz . Finally, for a multilayer comprising L layers, for any layer l_j we obtain the total dipolar field

$$\mathbf{H}_{\text{dip}}^{\text{tot},j} = \mathbf{H}_{\text{dip}}(\mathbf{m}_j, t_j, t_j, 0) + \sum_{i=1, i \neq j}^L \mathbf{H}_{\text{dip}}(\mathbf{m}_i, t_i, t_j, z_j - z_i), \quad (12)$$

where we separate the self-interacting term and the inter-layer interactions term, as they have different forms from Eq. (9).

With the model of magnetic interactions in multilayered skymion systems that we describe here, a tridimensional problem is thus reduced into a bidimensional problem, as the geometric variables are layers l_1, l_2, \dots, l_L and radius, which can be discretized in points r_1, r_2, \dots, r_N , with evident efficiency gain. The convergence time evolves with L^2, N^2 , the choice of initial guess and the required final precision. It allows the study of the profiles of multilayered skymions by direct numerical minimization. As we demonstrate below, it offers an efficient tool for understanding different issues related to the chirality of skymions in such multilayered systems. In order to focus on the presentation of the model without going too far into its technical aspects, we have actually skipped several details regarding its numerical implementation. However, we believe that it can be of interest to discuss some points of the implementation, as they are essential to get an accurate determination of the energy and a fast convergence of the model. An extended description of the implementation of the model is thus given in [Appendix B](#).

III. VALIDATION OF THE MODEL: COMPARISON WITH MUMAX³

Before using the present model to analyze the properties of isolated skymions in multilayers, we check the validity of our $\mathbf{m}(r)$ solver by comparing its results with the standard micromagnetic simulation package Mumax³ [44]. In the following, we will always consider multilayers with fixed layer thickness ($t_i = t_{\text{FM}}$ for all layers) and periodicity p between layers, even if we note that the model we have presented above can also be used to model the case of arbitrary layer thicknesses and positions. We select a set of standard parameters for Co-based multilayers [8]: $A = 10$ pJ m⁻¹, $D = 1.35$ mJ m⁻², $M_S = 1$ MA m⁻¹, $K_u = 0.8$ MJ m⁻³ (which corresponds to $K_{\text{eff}} = 0.172$ MJ m⁻³), $\mu_0 H_{\text{ext}} = 50$ mT, $t_{\text{FM}} = 1$ nm, and $p = 3$ nm. We initialize the magnetization in all layers with a usual approximation [26] of the skymion profile

$$\mathbf{m} = [\sin(\theta) \cos(\phi), \sin(\theta) \sin(\phi), \cos(\theta)],$$

$$\theta(r) = \frac{\pi}{2} - \arcsin \left[\tanh \left(\frac{r - 4\delta}{\delta} \right) \right], \quad \phi(r) = \pi/4, \quad (13)$$

where $\delta = \sqrt{A/K_{\text{eff}}}$ is the domain-wall width, and where the initial ϕ is chosen on purpose in between Bloch ($\phi = \pm\pi/2$) and Néel ($\phi = 0, \pi$) configurations, in order to let the system relax to its most stable state. Note that this initial configuration will determine the Bloch component of the magnetization texture (towards $\phi = \pi/2$) if any, but the solution with an opposite Bloch component (towards $\phi = -\pi/2$) is equally valid, because no interaction or sample geometry breaks this symmetry in the absence of bulk DMI. We let both algorithms (our solver and Mumax³) converge to $|\delta_{\mathbf{m}}| < 10^{-9}$ and compare the resulting profiles.

Before we analyze the results, we have to note that the two solvers actually treat two different problems. In our $\mathbf{m}(r)$ solver, we study an isolated skyrmion within an infinite, uniformly magnetized layer, whereas in the case of Mumax³, the simulated system always has a finite size and the magnetization outside it is only mimicked with periodic boundary conditions. To check that both methods agree in the limit of very large simulation sizes in Mumax (number of cells corresponding to one edge of the simulated square area, $N_{\text{mumax}} \rightarrow \infty$), we compare our model to different runs of Mumax³ with increasing simulation sizes $N_{\text{mumax}} = 256, 512, 768$. The cell size is fixed at $1 \times 1 \times 1 \text{ nm}^3$. We consider two geometries with $L = 3$ and $L = 5$ layers, for which we present the resulting skyrmion profiles in Figs. 2(a) and 2(b). In both cases, we find a very good agreement between our solver and Mumax³. Due to the large D , skyrmions are Néel with $\phi = 0$ in all layers. As we can see from the plots of layer-by-layer profiles $\theta(r)$ with increasingly large hollow squares, corresponding to increasing sizes of the simulation grid with $N_{\text{mumax}} = 256, 512, 768$, the skyrmion profile in the finite geometry of Mumax progressively converges to the skyrmion profile in the infinite geometry of the $\mathbf{m}(r)$ solver, represented by the lines. The difference of magnetization angles $\epsilon(r)$ between the $\mathbf{m}(r)$ solver and the results of the different runs of Mumax is represented in Fig. 2(c) for $L = 5$, which indeed shows a reducing difference when the number of cells in the Mumax grid is increasing. Note that the better definition of the profiles at small radii in the $\mathbf{m}(r)$ solver, which matches the geometry of the skyrmions, makes it more precise than a model based on a prismatic space such as Mumax for equivalent discretization sizes (here 1 nm^3). As a consequence, a small difference between profiles may remain in the limit of $N_{\text{mumax}} \rightarrow \infty$. We have also checked that the values of the effective fields found by both models are equal for $L = 3$ up to $L = 20$, and at different values of $\phi(r)$ angles.

IV. APPLICATION TO THE PROBLEM OF THE SIZE OF SKYRMIONS

Optimizing the magnetic properties of multilayers aiming at reducing the size of the skyrmions [36] is a crucial

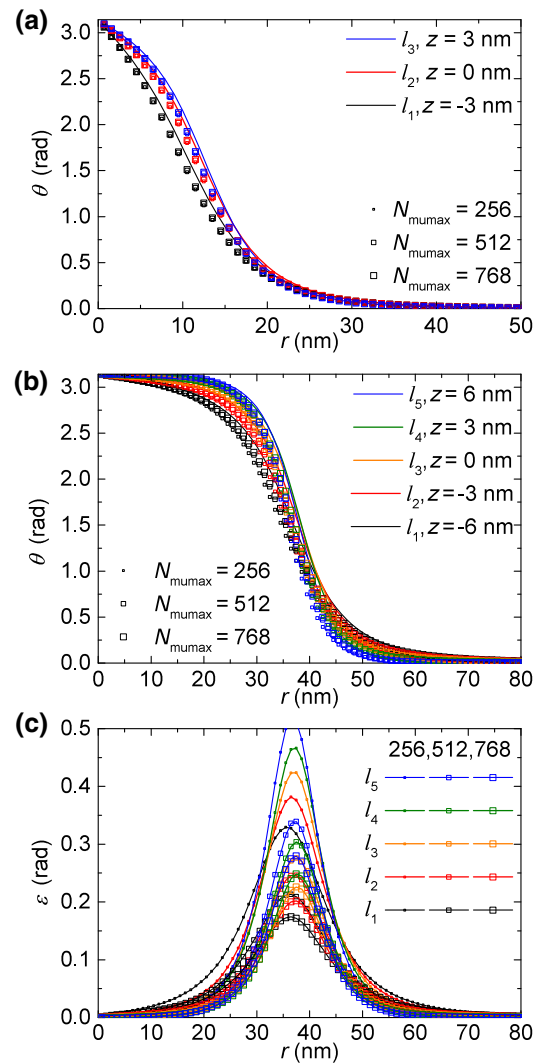


FIG. 2. Multilayer model comparison for (a) $L = 3$ and (b) $L = 5$ layers. Colored lines are the $\theta(r)$ profiles in each layer from our $\mathbf{m}(r)$ model, while hollow squares are the results from Mumax³ package. (c) Difference of $\theta(r)$ between models for $L = 5$. Layers are denoted by l_i with i increasing from bottom to top. The increasing sizes of the hollow squares correspond to the cases $N_{\text{mumax}} = 256, 512, 768$.

step towards scalable applications. In this section, we thus begin by a study of the equilibrium sizes (and profiles) of the skyrmion in each layer as a function of the external magnetic field H_{ext} . We first describe the cases of $L = 3$ and $L = 5$, for fields varying in the ranges $\mu_0 H_{\text{ext}} = 30\text{--}100$ and $50\text{--}150$ mT, respectively. Note that in our model the skyrmion is embedded in an infinite plane; in particular, there is no confinement due to the problem geometry or edge effects [43]. We only consider cases for which the finite simulation space does not influence the profile of skyrmions, that is, m_z very close to 1 at the maximum r_N considered.

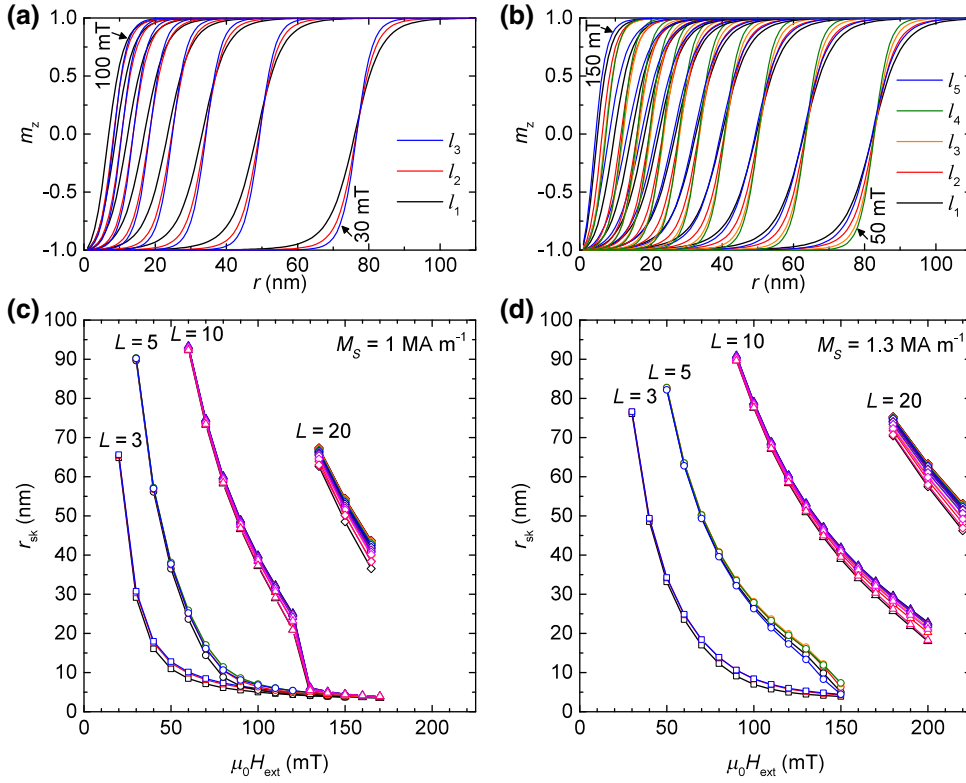


FIG. 3. Profile of the skyrmion at different external fields, by 10-mT increments, for (a) $L = 3$ and (b) $L = 5$ layers with $M_S = 1.3 \text{ MA m}^{-1}$. The different colors of lines are the $m_z(r)$ profiles in each layer. Layer-by-layer skyrmion radius r_{sk} as a function of external field, for $L = 3, 5, 10, 20$, in the cases of (c) $M_S = 1.0 \text{ MA m}^{-1}$ and (d) $M_S = 1.3 \text{ MA m}^{-1}$. The different colors distinguish between the different layers.

For this first example of application of our model, we use $M_S = 1.3 \text{ MA m}^{-1}$, $K_u = 1.2 \text{ MJ m}^{-3}$, and other parameters the same as above, which is typical of pure Co- and Fe-based ferromagnetic layers [33]. The obtained profiles are reported in Figs. 3(a) and 3(b). For increasing values of the external field, we notice an evolution from bubble skyrmions, which exhibit an extended core, at lower fields, towards compact skyrmions, at larger magnetic fields. As we can see from the different shapes of the profiles in each layer, they are differently affected by the external field, even for multilayers restricted to a few layers. To extend this study, we present the evolution of the skyrmion size in each layer as a function of the external field, for both $M_S = 1.0 \text{ MA m}^{-1}$; $K_u = 0.8 \text{ MJ m}^{-3}$ [Fig. 3(c)] and $M_S = 1.3 \text{ MA m}^{-1}$; $K_u = 1.2 \text{ MJ m}^{-3}$ [Fig. 3(d)], and multilayers with $L = 3, 5, 10, 20$. The skyrmion size r_{sk} is defined as the (layer-dependent) radius at which $m_z = 0$ (see Fig. 1).

As expected, the effects of the dipolar field are more and more pronounced when the number of repeated layers is increased. This appears very clearly in at least three ways. First, at a given radius, the curves of $r_{\text{sk}}(H_{\text{ext}})$ are shifted to higher fields for increasing L , because more confinement is required to prevent the skyrmion from expanding under the influence of dipolar interactions from more layers. Second, the slope of these curves at a given radius reduces with increasing L , which indicates that the external-field variations are less significant relative to the intrinsic dipolar field. Third, the split of the $r_{\text{sk}}(H_{\text{ext}})$ curves for the different

layers increases with L due to the increasing interlayer interactions. These trends are confirmed by comparing the results presented in Figs. 3(c) and 3(d), which shows that increasing M_S has a similar effect as increasing L , as it also results in a stronger dipolar field. For the case of $L = 20$, the skyrmion radius can thus vary by more than 20% between the external and the central layers of the stacking, resulting in a barrel shape for the skyrmion, as evidenced by the profiles in Fig. 4, corresponding to the case $M_S = 1.3 \text{ MA m}^{-1}$. As a consequence, it appears important to consider the impact of dipolar interactions and of the multilayered nature of such skyrmions in order to properly describe their profiles and sizes.

V. STABILITY OF ISOLATED SKYRMIONS AGAINST ANISOTROPIC DEFORMATIONS

Even if a skyrmion configuration may minimize the energy in the space of axisymmetric solutions, it may not be a minimum of energy if the symmetry constraint is relaxed. In particular, we have to check that the skyrmion solutions that we find are stable against anisotropic deformations [45], or equivalently, that the skyrmion deformation towards a stripe domain is energetically disfavored. To perform this verification, a first possibility is to add small perturbations to $\mathbf{m}(x, y, z)$ in the full, three-dimensional Cartesian micromagnetic model and let the system evolve, but this is computationally expensive. Here we propose, as an alternative approach, to

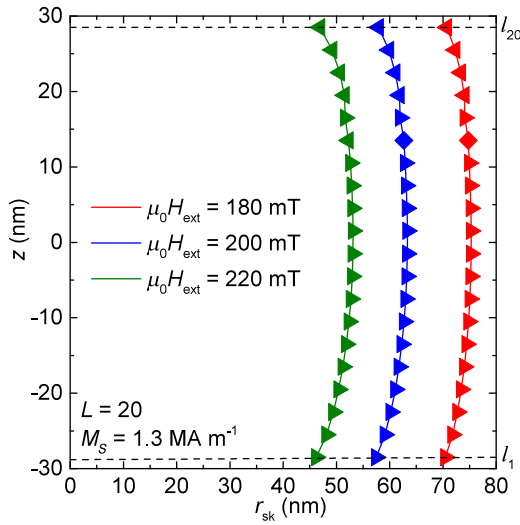


FIG. 4. Global structure of the skyrmion represented by its layer-dependent r_{sk} at different z positions for $L = 20$ layers, with $M_S = 1.3 \text{ MA m}^{-1}$, at different external fields $\mu_0 H_{\text{ext}} = 180 \text{ mT}$ (red curve), 200 mT (blue curve), and 220 mT (green curve). The vertical axis is the z position of the layers from l_1 at the bottom to l_{20} on the top. The effective chirality in each layer is represented by the shape of the symbols: right-pointing triangles for Néel chirality with $\phi = 0$, diamonds for intermediate configurations with $0 < \phi < \pi$ and left-pointing triangles for Néel chirality with $\phi = \pi$.

establish an approximate criterion for this stability by considering the energy of a stripe domain. Let us consider a domain profile $\mathbf{m}(x, z)$ with $\mathbf{m}(x, z) = \mathbf{m}(r, z)$ for $x = r > 0$ and its symmetric for $x < 0$, i.e., the same profile as a cut through the skyrmion core along the x direction, but uniform along the y direction. As this profile is suited to the cylindrical geometry of a skyrmion, we have to relax it to its most stable 360° -domain-wall form, proceeding with a similar energy minimization procedure as described above, but assuming instead a linear geometry (uniform along y). We provide in [Appendix D](#) the form of the stripe energy per unit length E_{st} , that we have used to find the stability of previously determined solutions. The total energy E'_{tot} is the sum of E_{st} in all layers. If the resulting stripe has a total energy lower than the saturated state, the system will decrease its energy through deformation of the skyrmion, splitting it into two half skyrmions (also called merons) located at the two ends of a stripe domain and thus the skyrmion will be unstable.

In [Fig. 5](#), we show the 360° -domain-wall energies obtained for all sets of magnetic parameters studied in [Figs. 3\(c\)](#) and [3\(d\)](#), with $M_S = 1.0 \text{ MA m}^{-1}$ (and $K_u = 0.8 \text{ MJ m}^{-3}$) in [Fig. 5\(a\)](#), with $M_S = 1.3 \text{ MA m}^{-1}$ (and $K_u = 1.2 \text{ MJ m}^{-3}$) in [Fig. 5\(b\)](#). We consider three different geometries $L = 3$, $L = 5$, and $L = 10$. As the usual single layer, single domain-wall energy per surface unit is $4\sqrt{AK_{\text{eff}}}$, the stripe energy, without DMI

and domain-domain dipolar interactions energy gain, for L layers, is around $8Lt_{\text{FM}}\sqrt{AK_{\text{eff}}}$. The stripe energy of the 360° -domain walls E'_{tot} is thus evaluated in units of $8Lt_{\text{FM}}\sqrt{AK_{\text{eff}}}$. When the DMI and dipolar interactions compensate for this domain-wall energy cost added to the Zeeman energy cost, $E'_{\text{tot}} < 0$ so that the stripe configuration is favored over the uniform state and the skyrmion expands into a stripe domain. We can see that $E'_{\text{tot}} < 0$ only at $\mu_0 H_{\text{ext}} = 30\text{--}40 \text{ mT}$ and $M_S = 1.3 \text{ MA m}^{-1}$ for $L = 3$, and in more cases for $L = 5$ or $L = 10$. For verification of this method, the stability as obtained from small perturbations to $\mathbf{m}(x, y, z)$ in the full, three-dimensional Cartesian micromagnetic model is also reported on these graphs by the interior of the symbols: hollow symbols correspond to unstable skyrmion configurations whereas filled symbols correspond to stable skyrmion configurations. A very good agreement is found, as the unstable configurations from the perturbation method match with negative values of minimized E'_{tot} in all cases tested here except for $L = 5$, $\mu_0 H_{\text{ext}} = 80 \text{ mT}$, and $L = 10$, $\mu_0 H_{\text{ext}} = 150 \text{ mT}$, for $M_S = 1.3 \text{ MA m}^{-1}$ only. In these cases, even if the stripe configuration is more stable than the uniform state, the energy gain associated to stripes is extremely small so that a weak energy barrier remains between the skyrmion configuration and the stripe configuration. The skyrmion thus has a very small stability, which would, however, not resist against thermal fluctuations. Finally, $E'_{\text{tot}} > 0$ is a satisfactory criterion to estimate the skyrmion stability against anisotropic deformations, that is, the validity of the solutions of our axisymmetric model.

Similar to $E'_{\text{tot}} > 0$ that indicates the stability of an isolated skyrmion state relative to the stripe state, we note that the calculation of whether $E_{\text{tot}} < 0$ provides the stability of an isolated skyrmion state relative to the uniform state. However, our model does not provide a direct estimation of the thermal metastability [\[36\]](#) of the calculated skyrmion states. We note that an interesting approach could be to use the calculated profiles to perform nudged elastic band calculations and to determine properly their stability against thermal fluctuations [\[46–48\]](#).

VI. CHIRALITY: DMI VS DIPOLAR INTERACTIONS

In the previous sections, we have focused on the layer-dependent size of the magnetic skyrmions, which has clearly shown how dipolar interactions affect the skyrmion profiles, and their stability. We now focus on the actual chirality of the multilayered skyrmions, and describe how the competition between interfacial DMI and dipolar interactions can result in hybrid chiral textures with different chiralities in the different layers. Importantly, we emphasize that such hybrid chiral configurations can be stabilized even for a limited number of repetitions L , as demonstrated hereafter.

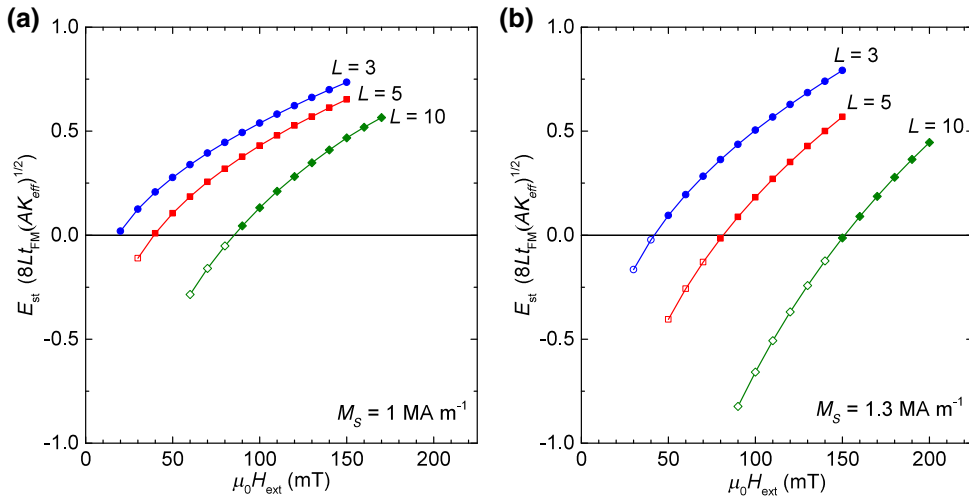


FIG. 5. Energy of the 360°-domain-wall stripe as a function of the external field, for $L = 3, 5, 10$, in the cases of (a) $M_S = 1.0 \text{ MA m}^{-1}$ and (b) $M_S = 1.3 \text{ MA m}^{-1}$. Circles correspond to $L = 3$, squares to $L = 5$, and diamonds to $L = 10$. The filled symbols correspond to stable skyrmions in full, tridimensional micromagnetic simulations, while hollow symbols correspond to unstable skyrmions (subject to strip-out instability) in full, tridimensional micromagnetic simulations.

We describe the case of a multilayer with $L = 3$ and low effective anisotropy K_{eff} , typical among room-temperature skyrmion systems. In such systems, the combination of low K_{eff} and nonzero DMI favors the rotation of the magnetization through the plane, which helps to stabilize skyrmions under the bias of the external magnetic field H_{ext} . The accumulation of three magnetic layers of relatively large thickness increases their stability. Here we consider $t_{\text{FM}} = 1.4 \text{ nm}$ and $p = 3.4 \text{ nm}$; $M_S = 1.3 \text{ MA m}^{-1}$; $K_u = 1.2 \text{ MJ m}^{-3}$. In order to study quantitatively the competition between dipolar interactions and DMI, we vary the DMI magnitude between $D = -1.8 \text{ mJ m}^{-2}$ and $D = 1.8 \text{ mJ m}^{-2}$. Note that $D = 1.35 \text{ mJ m}^{-2}$ is the largest effective value of D that has been achieved experimentally [33] for magnetic layers as thick as 1.4 nm. In order to highlight the importance of considering a layer-by-layer description for this kind of multilayer, we compare in Fig. 6 the results of our model (called Layer-by-layer) to the results of a simpler model (called Uniform), in which we impose that all layers share the same profile [36]. In each panel, one cell of the grid corresponds to one set of $(D, \mu_0 H_{\text{ext}})$ parameters. In the panels of the layer-by-layer description, each cell of the grid actually shows the results of the model for the three different layers.

First, the results for the size of the skyrmion are shown in Figs. 6(a) and 6(b) for the Uniform model and the Layer-by-layer model, respectively. As before, for the layer-by-layer case r_{sk} is defined as the (layer-dependent) radius at which $m_z = 0$. In the present case, a very small layer-by-layer variation of the skyrmion size is found in our model, as shown by the almost uniform color in each cell of the panel in Fig. 6(b). However, the skyrmion size dependence is much less abrupt in our model than in the uniform model, and leads to fewer cases for which the skyrmion collapses (r_{sk} below the cell size of 1 nm, in gray). This is due to the complete modeling of the interlayer interactions and difference of magnetization profiles between layers. The extra degree of liberty given by the

possibility of layer-by-layer variations of the magnetization allows the system energy to be reduced and keeps stable skyrmions in a larger range of parameters. Second, the average value $\langle \phi \rangle$ of the in-plane azimuthal angle (later on called effective chirality) of the skyrmion in each layer are shown in Figs. 6(c) and 6(d) for the uniform model and the layer-by-layer model, respectively. For the case of the layer-by-layer description, the three layers from bottom to top are represented by the three stacked colors in each cell. Whereas the D dependence of the chirality is, as expected, nearly linear [36,49] for the uniform model description [in Fig. 6(c), the color indicating the chirality evolves linearly from the center to the sides of the figure], it is no longer linear for the refined layer-by-layer description [in Fig. 6(d)].

When all layers are considered individually, the effective chiralities of the skyrmion in the different layers thus evolve depending on D through different steps. In the absence of DMI, only dipolar field is present, which is able to reorientate the skyrmions of the bottom and top layers into Néel skyrmions of opposite chiralities instead of Bloch skyrmions, while the skyrmion of the central layer remains Bloch [central column of Fig. 6(d)]. When a small DMI is progressively added, the chirality of the skyrmion in the central layer progressively evolves towards Néel of the chirality determined by the sign of the DMI. For the central layer, this is the same scenario as in the single-layer case, where the intralayer dipolar interactions are progressively overcome by the DMI. Finally, to reorientate the last remaining Néel skyrmion of chirality opposed to the one favored by DMI (either located in the top or bottom layer depending on the sign of D), the interlayer dipolar interactions must also be overcome, rather than only the intralayer dipolar interactions. This shifts the reversal of chirality in the last layer to much larger values of D . As can be seen in Fig. 6(d), for the lowest field value, $|D| \geq 1.2 \text{ mJ m}^{-2}$ is required for the chirality of the last layer skyrmion to evolve. For $|D| \geq 1.65 \text{ mJ m}^{-2}$, a Néel

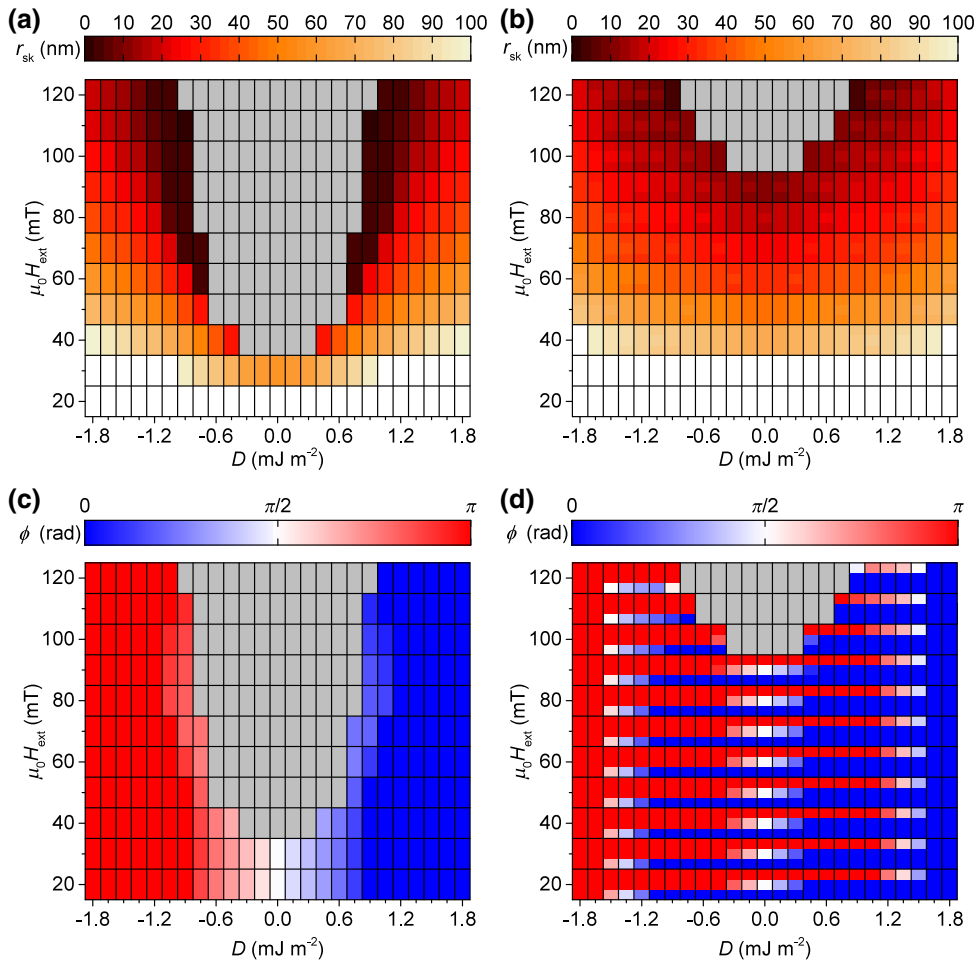


FIG. 6. Equilibrium size of the skyrmion as a function of DMI parameter and external field, for (a) a model with uniform magnetization through the thickness and (b) a layer-by-layer description. The size corresponding to the color in each cell is given by chirality, given by the average in-plane angle of the magnetization with respect to the radial direction, for (c) a model with uniform magnetization through the thickness and (d) a layer-by-layer description. As introduced before, $\phi = 0$ means a Néel skyrmion with counter-clockwise chirality, $\phi = \pi/2$ means a Bloch skyrmion and $\phi = \pi$ means a Néel skyrmion with clockwise chirality, as given by the color scale. Gray signifies that the skyrmion collapses below the cell size for these parameters. For the layer-by-layer model, inside a cell of the grid, which corresponds to a single set of parameters, the three stacked colors from bottom to top correspond to the three layers from bottom to top.

skyrmion with a uniform chirality in accordance with the sign of the DMI is recovered. The competition between DMI and dipolar interactions occurs very similarly when L is increased, shifting the reversal of chirality to higher values of $|D|$ in all but the central layer (if any, only for odd values of L). As such reorientation effects are due to the dipolar field, an even higher value of D is required to get a uniform chirality for larger values of M_S , for larger layer thicknesses, and for larger values of L (see Discussion in Sec. VIII). Note that the present case has been chosen to highlight the role of the dipolar field, choosing large M_S and thick ferromagnetic layers.

For the case of $L = 20$ that has been studied in Sec. IV, the effective chirality in each layer is shown by the shape of the symbols in Fig. 4. Layers l_1 – l_{14} are Néel with $\phi = 0$ (right-pointing triangles), layers l_{17} – l_{20} are Néel with $\phi = \pi$ (left-pointing triangles), and a transition occurs in layers l_{15} and l_{16} (with diamonds for Bloch or partially Bloch). The complex transition, not being always simply Néel to Bloch to opposite Néel, but being in some cases a succession of alternating chiralities, seems to be a complex consequence of the shape of the dipolar field. It is confirmed by full micromagnetic simulations using

Mumax³. Even for a value of D as high as 1.35 mJ m^{-2} , as in the present case, one fourth of the layers are still hosting Néel skyrmions with an effective chirality opposed to the one favored by the DMI, similar to what was found experimentally in a previous work [24].

VII. APPLICATION TO THE CURRENT-DRIVEN DYNAMICS OF HYBRID CHIRAL SKYRMIONS

From the energy minimized $\theta_i(r)$ and $\phi_i(r)$ profiles in all layers obtained above, the expected skyrmion velocities can be directly predicted by making use of the Thiele formalism. In the Thiele approach, the skyrmion is considered as a rigid object, and the global forces acting on the skyrmion can be expressed from the Landau-Lifshitz-Gilbert equation, by integrating the torques acting on the magnetization over the whole magnetization texture [12,50,51]. For an axisymmetric skyrmion of profile $\mathbf{m} = (m_r, m_\phi, m_z)$ we have

$$\mathbf{G} \times \mathbf{v} - \alpha [D] \mathbf{v} + \mathbf{F} = \mathbf{0}, \quad (14)$$

with

$$\begin{aligned} \mathbf{G} &= -\frac{M_S t_{\text{FM}}}{\gamma} \iint \left(\frac{\partial \mathbf{m}}{\partial x} \times \frac{\partial \mathbf{m}}{\partial y} \right) \cdot \mathbf{m} \, dx dy z, \\ [\mathcal{D}] &= \begin{bmatrix} \mathcal{D}_{xx} & \mathcal{D}_{xy} \\ \mathcal{D}_{yx} & \mathcal{D}_{yy} \end{bmatrix}, \quad \mathcal{D}_{ij} = \frac{M_S t_{\text{FM}}}{\gamma} \iint \left(\frac{\partial \mathbf{m}}{\partial i} \cdot \frac{\partial \mathbf{m}}{\partial j} \right) dx dy, \\ F_{x,y} &= \frac{\mu_0 M_S t_{\text{FM}}}{\gamma} \iint (\mathbf{m} \times \boldsymbol{\Gamma}) \cdot \frac{\partial \mathbf{m}}{\partial x,y} dx dy, \end{aligned} \quad (15)$$

where \mathbf{G} is the gyrovector, γ is the gyromagnetic ratio, α is the Gilbert damping parameter, $[\mathcal{D}]$ the dissipation matrix, \mathbf{v} the skyrmion velocity, and \mathbf{F} the force exerted on the skyrmion magnetization by the torque $\boldsymbol{\Gamma}$. In the present example, we model the injection of a vertical spin current polarized along y , which exerts a torque $\boldsymbol{\Gamma}_{\text{SOT}}$. For simplicity, we only consider a dampinglike component, as the fieldlike component may deform the skyrmion but shall not move it, in the first approximation. This would correspond, for example, to the case of a spin Hall effect due to a charge current flowing along x in the multilayer. As we consider an axisymmetric skyrmion with $m_z(0) = -\mathbf{z}$ and $m_z(\infty) = +\mathbf{z}$ (see Fig. 1), it results that off-diagonal terms in $[\mathcal{D}]$ are zero and

$$\begin{aligned} \mathbf{G} &= 4\pi \frac{M_S t_{\text{FM}}}{\gamma}, \\ \mathcal{D}_{xx,yy} &= \pi \frac{M_S t_{\text{FM}}}{\gamma} a, \\ F_{x,y} &= \mp \theta_{\text{SH}} J \frac{\pi \hbar}{2e} b_{x,y}, \end{aligned} \quad (16)$$

where a is a dimensionless coefficient related to the magnetic structure of the skyrmion; J is the in-plane charge-current density in the multilayer, and θ_{SH} is the effective spin Hall angle; b_x and b_y are homogeneous to different characteristic sizes of the skyrmion, related to their geometry and magnetic structures, defined as

$$\begin{aligned} a &= \int_{r=0}^{\infty} \frac{1 - m_z^2}{r} + r \sum_{i=x,\varphi,z} \left(\frac{\partial m_i}{\partial r} \right)^2 dr, \\ b_x &= \int_{r=0}^{\infty} r \left(\frac{\partial m_r}{\partial r} m_z - \frac{\partial m_z}{\partial r} m_r \right) + m_r m_z dr, \\ b_y &= \int_{r=0}^{\infty} r \left(\frac{\partial m_\varphi}{\partial r} m_z - \frac{\partial m_z}{\partial r} m_\varphi \right) + m_\varphi m_z dr, \end{aligned} \quad (17)$$

where details of the derivation are given in [Appendix E](#). We note that the formalism provided by the Thiele equation is not able to treat the effect of deformations of skyrmions. As a consequence, the following conclusions are valid for small, compact skyrmions at low current densities, but may be altered for more deformable, plateau

skyrmions (with a uniform magnetization core of finite size) at higher current densities. Also, we consider low enough currents so that no deformations in the vertical dimension of the columnar skyrmions occurs, even when they are driven with different spin injections in the different layers. At higher current densities, magnetic skyrmions would break their axial symmetry, and could even be destroyed by the different torques obtained in different layers, which is beyond what can be described by the present model.

As can be seen from (17), the direction of the force driving the current-induced motion is directly set by the texture and chirality of the skyrmion: a Néel skyrmion is driven by a force along the x direction while a Bloch skyrmion is driven by a force along the y direction, with the sign of the force being determined by the chirality. As a consequence, the layer-dependent chirality obtained in the layer-by-layer approach is crucial to model correctly the current-induced motion of hybrid chiral skyrmions.

We present in Fig. 7 the results of the Thiele modeling for a system identical to the one of the previous section ($L = 3$). We consider a multilayer geometry in which a similar spin current of magnitude given by $\theta_{\text{SH}} J = 2 \times 10^{10} \text{ A m}^{-2}$ is injected into each ferromagnetic layer, which would correspond to the case of having an identical heavy-metal layer adjacent to each ferromagnetic layer. The obtained effective forces F_x [Figs. 7(a) and 7(b)] and F_y [Figs. 7(c) and 7(d)] due to current-induced torques are the direct consequence of the average of the chirality in all layers shown in Figs. 6(c) and 6(d). We thus compare again a model with uniform magnetization through the thickness [Figs. 7(a) and 7(c)] and the Layer-by-layer model [Figs. 7(b) and 7(d)]. We find, in the case of layer-by-layer modeling, that the driving force is maximized for a uniform chirality, while it is strongly reduced for a hybrid chirality, due to Néel skyrmions with opposite chiralities. Indeed, in the latter case, top and bottom layer skyrmions, showing opposite chiralities, are driven in opposite directions. This is the main reason for the large difference in the magnitude of the driving forces between the two models. Because the uniform model fails to predict and describe the hybrid chirality, and hence neglects the competing current-induced forces arising in the top and bottom layers, it largely overestimates the effect of the spin currents on the global structure for all values of D that are not large enough to ensure a unique chirality in the whole stack of layers.

VIII. DISCUSSION

For several applications of magnetic skyrmions, such as shift-register memories or logic devices [19], a fast current-induced propagation of the information carried by the skyrmions is desired. We have recently shown the importance of taking into account the spin-torque symmetries with respect to the effective skyrmion chiralities in

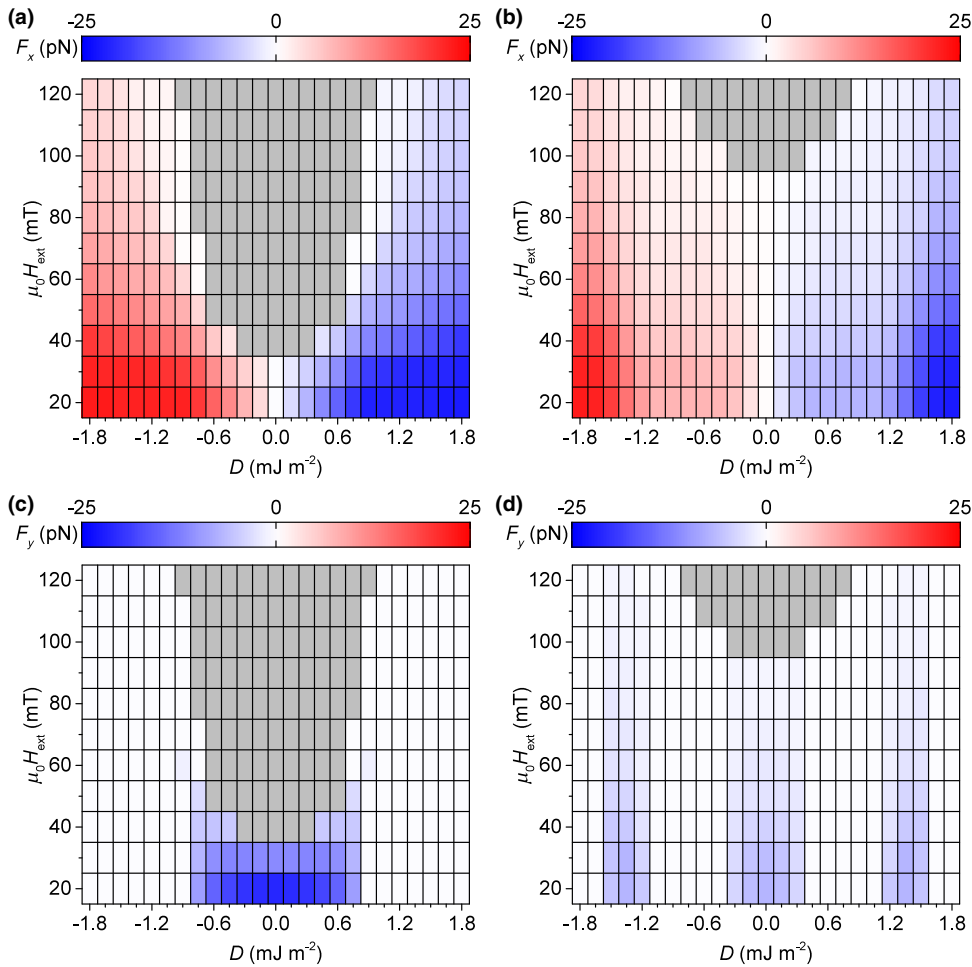


FIG. 7. Forces acting on the skyrmion due to the spin-orbit torques as a function of DMI parameter and external field, along x for (a) a model with uniform magnetization through the thickness and (b) a layer-by-layer description, along y for (c) a model with uniform magnetization through the thickness and (d) a layer-by-layer description. The sign and magnitude of the force is given by the color scale. Gray signifies that the skyrmion collapses below the cell size for these parameters.

multilayers in order to achieve a fast propagation of the skyrmions [24]. Beyond the case of this simple, pedagogical example of a uniform current injection geometry with $L = 3$ (see Fig. 7), our model can be used to investigate any type of spin-current injection scheme in multilayers, allowing us to predict the dynamics of skyrmions and discriminate the interesting configurations among a very large choice of possible experimental multilayered structures. For example, we consider here different spin-current injection geometries in the case of a complex, hybrid skyrmion as found for $L = 20$ and $\mu_0 H_{\text{ext}} = 200$ mT (Fig. 4). The spin-current magnitude is again $|\theta_{\text{SH}} J| = 2 \times 10^{10}$ A m^{-2} in all cases. The obtained forces are shown in Fig. 8.

In the first geometry (labeled as “Ident.” in Fig. 8), the spin currents generate an identical spin accumulation in the bottommost (l_1) and topmost layers (l_{20}) only. This situation corresponds, for example, to spin-orbit torques existing in multilayers being enclosed between two heavy-metal layers of opposite spin Hall angles (e.g., Pt and Ta), with negligible spin torques generated inside the multilayer. In this geometry, due to the hybrid chirality, the forces exerted on the top and bottom parts of the skyrmion cancel each other so that the total force drops to zero. In

the second geometry (labeled as “Opp.” in Fig. 8), opposite spin injections occur at the top and bottom layers of the multilayer. This situation corresponds, for example, to spin-orbit torques existing in multilayers being enclosed between two heavy-metal layers of identical spin Hall angles. In this geometry, due to the hybrid chirality, the forces exerted on the top and bottom parts of the skyrmion add up so that the resulting force becomes significant. In the third geometry (labeled as “Optim.” in Fig. 8), the sign of the spin injection is designed to match the effective chirality in each layer as it is shown in Fig. 4. This can be achieved by inserting a heavy metal of the appropriate sign of spin Hall angle adjacent to each ferromagnetic layer. In this case, the torques are optimized and result in an about tenfold increase of the skyrmion driving forces as all layers (except l_{15} hosting a Bloch skyrmion) now contribute to the total force. In the last studied geometry (labeled as “Unif.” in Fig. 8), the spin injection is identical in all layers. This is simpler to achieve as it consists in repeating the same heavy metal adjacent to each ferromagnetic layer. The total force resulting of all layer-dependent forces thus reflects the balance between layers hosting Néel skyrmions with $\phi = 0$ and $\phi = \pi$. In this case, the driving

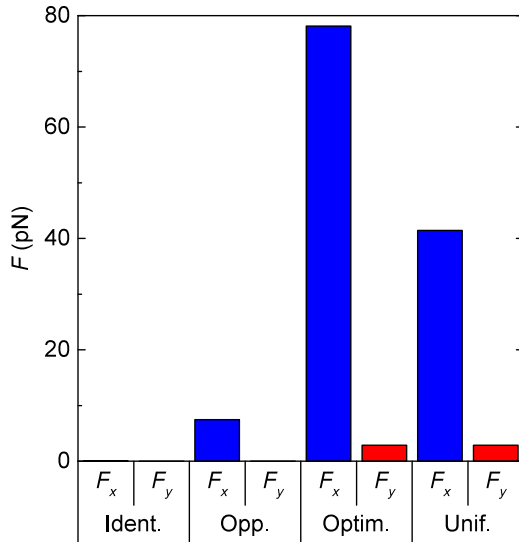


FIG. 8. Forces F_x and F_y acting on the multilayered hybrid chiral skyrmion due to the spin-orbit torques in different geometries of spin injection, for the case of $L = 20$ and $\mu_0 H_{\text{ext}} = 200$ mT.

force is reduced by half as compared to the previous case, as only ten layers contribute to the total force, while the forces exerted in the five bottommost and five topmost layers, hosting skyrmions of opposite chiralities, cancel each other. In the last two cases, a small force directed along y results from the Bloch part of the multilayered skyrmion, located in one of the intermediate layers. Note that the forces are much weaker for the geometry “Opp.” than for “Optim.,” because for “Opp.” the spin currents act on two layers only (topmost and bottommost), rather than on all 20 layers. If multiplied by this factor of 10, F_x for “Opp.” is about F_x for the “Optim.” geometry. These results, using the Thiele formalism, are in excellent agreement with our recent tridimensional micromagnetic simulations [24].

In the most accessible experimental situation that is described by the geometry “Unif.,” it is thus necessary to ensure a unique skyrmion chirality when aiming at maximizing the resulting skyrmion velocity for applications. To obtain a uniform Néel skyrmion chirality in all layers, the requirement is that $|D|$ be larger than D_u , its threshold value allowing the DMI to overcome the dipolar interactions even in the most external layers l_1 and l_L . Finding D_u in link with the multilayer geometry and the magnetic parameters is thus of great importance, prior to attempting any particular geometry for spin injection. We present examples of how D_u evolves with the number of layers L (keeping $M_S = 1.3$ MA m $^{-1}$) in Fig. 9(a), and how it evolves with M_S (keeping $L = 3$ and a constant effective anisotropy field $\mu_0 H_{\text{anis}} = 2K_{\text{eff}}/M_S = 212$ mT) in Fig. 9(b). For each geometry and value of M_S , the external field $\mu_0 H_{\text{ext}}$ is also varied, together with D , in order to compensate the effect of variations of DMI and dipolar interactions on the skyrmion size. All deduced values of

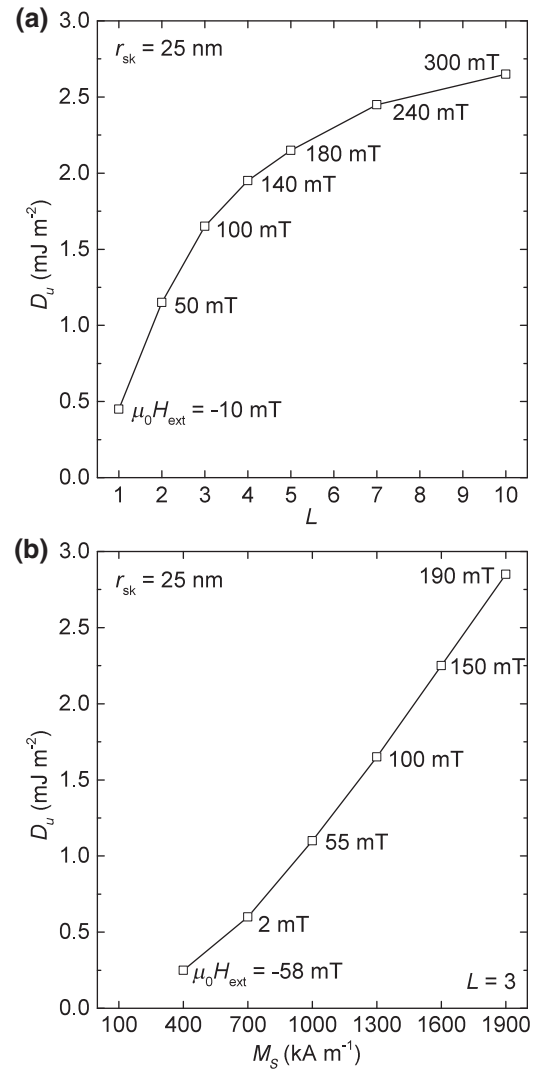


FIG. 9. Threshold DMI value D_u to ensure uniform skyrmion chirality (a) as a function of L for a fixed value of $M_S = 1.3$ MA m $^{-1}$ and (b) as a function of M_S for a fixed value of $L = 3$. The external field value $\mu_0 H_{\text{ext}}$ is varied in each case, and displayed along the curves, to allow comparison between skyrmions of constant size $r_{\text{sk}} = 25$ nm.

D_u are thus given for skyrmions of constant size $r_{\text{sk}} = 25$ nm, and thus similar magnetization profiles, which allows for a more pertinent comparison. As expected, D_u is found increasing with both L and M_S , due to increasing strength of dipolar interactions. As a consequence of the fast decay with distance of the dipolar field generated in a distant layer, D_u increases less and less rapidly at larger L , and appears to progressively saturate. In contrast, the dipolar field immediately scales with M_S , which results in the steady increase of D_u at the largest values of M_S . These results provide guidelines allowing to target, at choice, multilayers hosting skyrmions with hybrid chirality, or with uniform chirality.

Another important issue related to the applicability of magnetic skyrmions arises from the detrimental consequences of the skyrmion Hall effect, that is, of their side motion relative to external forces. Due to the particular topology of the magnetic skyrmions, as materialized by the gyrovecteur \mathbf{G} in the Thiele equation analysis presented above, the motion of a skyrmion does not occur in the direction of the driving force but with a certain angle. In nanotracks where Néel skyrmions would have been expected to be driven efficiently by spin-orbit torques, skyrmions are actually deflected towards the edges of the tracks, which may eventually lead to their annihilation due to edge interactions [52]. Kim *et al.* [53] have very recently suggested that the trajectory of skyrmions relative to the applied current could be engineered in hybrid-DMI systems, showing DMI of both bulk and interfacial origin, thus favoring neither pure Bloch nor pure Néel skyrmions. Most notably, it would be possible in these systems to cancel out the skyrmion Hall effect. Here, our model suggests that even in the case of a uniform, purely interfacial DMI, the presence of hybrid chirality can be exploited to control the skyrmion Hall angle of multilayered skyrmions. To support this statement, we use the forces as determined from the Thiele equation in the previous section, displayed in Fig. 7, in order to find the skyrmion velocity and skyrmion Hall angle in the simple case of $L = 3$ with a uniform spin injection in all layers.

First, we display in Fig. 10(a) both v_x (black, thick lines) and v_y (red, thin lines) as a function of Gilbert damping α , obtained by solving (14) for $D = 1.35 \text{ mJ m}^{-2}$ and $\mu_0 H_{\text{ext}} = 50 \text{ mT}$ [see the corresponding skyrmion configuration in Figs. 6(b) and 6(d), and forces in Figs. 7(b) and 7(d)]. We consider two cases depending on the chiral configuration of the top layer. Indeed two configurations are actually degenerate in energy, for negative values (dashed-dotted lines) and positive values (solid lines) of the angle $\phi(r)$, which corresponds to the Bloch component of the skyrmion having one chirality or the other (still, the chirality of the Néel component is fixed by the DMI). The values of the forces F_x and F_y are constant and determined by the texture of the skyrmion. In addition, depending on whether $\phi > 0$ or $\phi < 0$, the transverse force F_y changes sign. Overall, in combination with the effect of the gyrotropic term that rotates the direction of motion, both v_x and v_y evolve significantly with α . Actually, the motion is deflected by an angle in between 90° (in the limit of $\alpha \rightarrow 0$) and 0° (in the limit of $\alpha \rightarrow \infty$). As a result, in one case v_y crosses zero. This appears clearly in Fig. 10(b), which displays the skyrmion velocity v (left axis, in blue) and the skyrmion Hall angle Θ_{sk} (right axis, in red) as a function of α . In the case of $\phi > 0$, for $\alpha \approx 0.35$, the skyrmion Hall effect is canceled while a significant velocity is still achieved. Considering the consequence of the hybrid chirality of skyrmions on their dynamics thus provide a means of canceling the undesired,

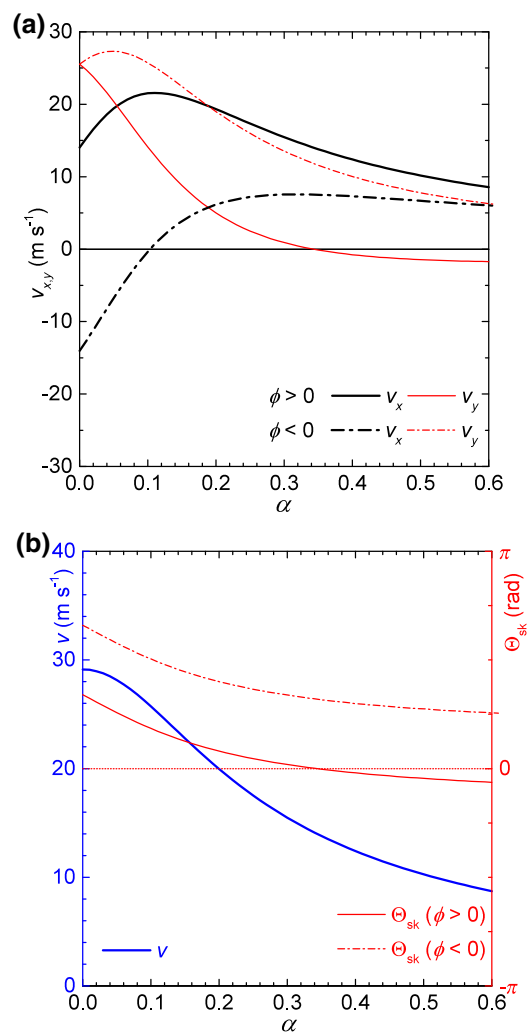


FIG. 10. (a) Longitudinal v_x (black, thick lines) and transverse v_y (red, thin lines) velocities as a function of the Gilbert damping α , for a hybrid chiral skyrmion with $\phi < 0$ (dashed-dotted lines) and $\phi > 0$ (solid lines). (b) Skyrmion velocity v (left scale, thick blue line), and skyrmion Hall angle Θ_{sk} (right scale, red thin lines) for a hybrid chiral skyrmion with $\phi < 0$ (dashed-dotted lines) and $\phi > 0$ (solid lines).

transverse motion. By combining this approach with the engineering of the spin-injection geometry, a high degree of control on the trajectories can be achieved.

We also believe that our model constitutes an important guiding tool in order to further reduce the size of magnetic skyrmions towards devices with higher integration density, considering simultaneously all aspects among detailed layer-by-layer magnetization profile, stability, and optimal spin-current injection for motion. As can be seen from the difference between Figs. 6(a) and 6(b), the predicted sizes and field stability of the skyrmions differ considerably depending on whether the multilayered nature of the skyrmions is considered. From an application point of view, our model allows accurate prediction of some of

the most important skyrmion properties for different multilayer compositions. It will thus allow optimization of the material design of skyrmion multilayers, which opens the way for the development of various skyrmion-based devices, going from skyrmion racetrack memories [19] to neuro-inspired component architectures [20,21].

IX. SUMMARY

In conclusion, we propose a Layer-by-layer model, which is able to predict accurately the actual profile of multilayered magnetic skyrmions and to describe the effects of interlayer dipolar interactions on the skyrmion size, stability, and chirality. Notably, this model is extremely suitable to study hybrid chirality through the magnetic layers of multilayered systems. Using the Thiele formalism, we have shown how this model can be used to predict the skyrmion velocity and skyrmion Hall angle under current-driven motion for any kind of spin-current injection scheme.

Even if we have focused here on the case of multilayers made of repetitions of a unique base of identical layers [identical ferromagnetic element(s), layer thicknesses, and spacer thicknesses and materials], we note that it can also be used to model the case of layer-by-layer varying magnetic parameters inside a stacking of different ferromagnetic layers. By including direct exchange between contiguous layers, and other forms of DMI, this model could also be easily adapted to the description of thick skyrmions in chiral magnets [11,23].

The present model can also be easily further refined by adding any other magnetic interaction, which opens the perspective of describing accurately more specific systems. For example, considering interlayer couplings mediated by electrons would allow the case of thin metallic spacers to be treated with RKKY interactions and thus the cases of coupled bilayers or antiferromagnetically coupled layers [31,54].

Obtaining the accurate layer-by-layer profile of the multilayered skyrmions shall also have implications, for example, on their electrical detection using their magnetic texture [55–57] or even on their thermodynamical stability [46–48].

ACKNOWLEDGMENTS

This work was partially supported by the Agence Nationale de la Recherche, France, under Grant Agreement No. ANR-17-CE24-0025 (TOPSKY), by the Horizon 2020 Framework Programme of the European Commission, under Grant Agreement No. 665095 (MAGicSky), and the DARPA TEE program through Grant No. MIPR# HR0011831554.

Note added.—A study by I. Lemesh et al. presenting an analytical model to describe similar three-dimensional magnetic skyrmions has been recently published [58].

APPENDIX A: SOLUTION FOR THE MAGNETIC POTENTIAL

Solution for $\bar{\psi}_f$. We consider as a general solution

$$\bar{\psi}_f = \begin{cases} B_1 \cosh(kz) + B_2 \sinh(kz) + B_0, & \text{inside,} \\ A_1 \exp(kz) + A_2 \exp(-kz) + A_0, & z > t/2, \end{cases} \quad (\text{A1})$$

for the inside and outside parts, respectively, with $A_{0,1,2}$, $B_{0,1,2}$ real constants. Using (i), we find that $B_0 = -\bar{f}(k)/k^2$ and $A_0 = 0$. Condition (ii) yields $A_1 = 0$. Using the symmetry with respect to z of volume charges, we get that $\bar{\psi}_f = A_2 \exp(kz)$, $z < -t/2$, and $B_2 = 0$. Combining (iii) and (iv) at $z = t/2$ we find

$$\begin{cases} B_1 \cosh(kt/2) - \bar{f}(k)/k^2 = A_2 \exp(-kt/2), \\ kB_1 \sinh(kt/2) = -kA_2 \exp(-kt/2), \end{cases} \quad (\text{A2})$$

which finally gives A_2 and B_1 .

Solution for $\bar{\psi}_h$. We consider as a general solution

$$\bar{\psi}_h = \begin{cases} B_1 \cosh(kz) + B_2 \sinh(kz) + B_0, & \text{inside,} \\ A_1 \exp(kz) + A_2 \exp(-kz) + A_0, & z > t/2, \end{cases} \quad (\text{A3})$$

for the inside and outside parts, respectively, with $A_{0,1,2}$, $B_{0,1,2}$ real constants. Using (i), we find that $B_0 = 0$ and $A_0 = 0$. Condition (ii) yields $A_1 = 0$. Using the antisymmetry with respect to z of surface charges, we get that $\bar{\psi}_h = -A_2 \exp(kz)$, $z < -t/2$, and $B_1 = 0$. Combining (iii) and (iv) at $z = t/2$ we find

$$\begin{cases} B_2 \sinh(kt/2) = A_2 \exp(-kt/2), \\ kB_2 \cosh(kt/2) + \bar{h}(k) = -kA_2 \exp(-kt/2), \end{cases} \quad (\text{A4})$$

which finally gives A_2 and B_2 .

APPENDIX B: CONSIDERATIONS FOR NUMERICAL IMPLEMENTATION

A first difficulty is the correct and efficient implementation of the Hankel transform. Indeed, the Bessel functions are slowly decaying and the use of a large set of values of k is required for a correct reconstruction of the functions. In case of undersampling, the Hankel transform is no longer involutive and $\bar{\bar{\psi}} \neq \psi$, which conveys wrong results. For the implementation of the Hankel transform, it is a good idea to choose sampling r points related to the position of the zeros of the Bessel functions [59]. This way, it is possible to obtain very accurate transforms even for a number of k points equal to the number of r points and relatively steep functions. Such a method has been tested and validated.

Whether a regular spacing or a specific choice of r points is chosen, we note that the use of functions for which $\int_0^\infty |g(x)| x^{1/2} dx$ converges is required. For isolated

skyrmions, which have a limited radius and are stabilized in an otherwise uniformly magnetized layer, for example along $+\mathbf{z}$, this is the case of f , but not h . For this reason, we define $\tilde{h} = M_S(1 - \mathbf{m} \cdot \mathbf{z})$, the surface charges associated to the difference $\mathbf{m}(r) - \mathbf{m}_{\text{unif}}(r)$ with $\mathbf{m}_{\text{unif}}(r) = \mathbf{z}$ the uniform magnetization. This new \tilde{h} function equals zero outside the skyrmion and has a properly defined transform. As the dipolar field associated to a source $\mathbf{m}_{\text{unif}}(r)$ is confined inside the layer and is equal to $-M_{SZ}$, by summing the two source terms $\mathbf{m}(r) - \mathbf{m}_{\text{unif}}$ and $\mathbf{m}_{\text{unif}}(r)$ we find that

$$\mathbf{H}_{\text{dip}} = \begin{cases} \tilde{\mathbf{H}}_{\text{dip}} - M_{SZ}, & -t/2 \leq z \leq t/2, \\ \tilde{\mathbf{H}}_{\text{dip}}, & |z| > t/2, \end{cases} \quad (\text{B1})$$

with $\tilde{\mathbf{H}}_{\text{dip}}$ the partial field obtained by replacing h by \tilde{h} .

The energy of the system includes the dipolar term, which is a long-range interaction and has an infinite extension. For an isolated skyrmion, a part of the stabilizing dipolar energy thus comes from the interaction with magnetic moments located towards infinity. However, for numerical implementation we have to consider a finite-size simulation space. We suppose N points $r_1, r_2, \dots, r_N > 0$, and as boundary conditions, that $\mathbf{m} = -\mathbf{z}$ at $r = 0$ and $\mathbf{m} = \mathbf{z}$ for $r > r_N$. With our definition of E_{sk} , the integrand of (1) is zero for $r > r_N$ with $\mathbf{m} = \mathbf{z}$, except for the dipolar energy term, due to the long-range nature of dipolar interactions. In order to be able to find the energy of the system, we then have to transform this expression in order to find an integrand, which becomes zero for $r > r_N$. We separate the system into two parts, interior with variable \mathbf{m} for $r \leq r_N$ and exterior with fixed \mathbf{m} for $r > r_N$. We can write

$$\mathbf{E}_{\text{dip}} = \left(\int_{\text{int}} + \int_{\text{ext}} \right) \frac{-\mu_0 M_S}{2} (\mathbf{H}_{\text{var}} + \mathbf{H}_{\text{fix}}) \cdot \mathbf{m}, \quad (\text{B2})$$

with \mathbf{H}_{var} the field generated by the interior part and \mathbf{H}_{fix} the field generated by the exterior part. In the exterior part, both \mathbf{m} and \mathbf{H}_{fix} are fixed, so that their scalar product is constant and can be dropped. We then keep

$$\mathbf{E}_{\text{dip}} = \frac{-\mu_0 M_S}{2} \left[\int_{\text{int}} (\mathbf{H}_{\text{var}} + \mathbf{H}_{\text{fix}}) \cdot \mathbf{m} + \int_{\text{ext}} \mathbf{H}_{\text{var}} \cdot \mathbf{m} \right] \quad (\text{B3})$$

and, as it is an interaction between two subsystems, we get that

$$\int_{\text{ext}} \mathbf{H}_{\text{var}} \cdot \mathbf{m} = \int_{\text{int}} \mathbf{H}_{\text{fix}} \cdot \mathbf{m} \quad (\text{B4})$$

so that we can write

$$\mathbf{E}_{\text{dip}} = \frac{-\mu_0 M_S}{2} \int_{\text{int}} \mathbf{H}_{\text{dip}} \cdot \mathbf{m} + \mathbf{H}_{\text{fix}} \cdot \mathbf{m}. \quad (\text{B5})$$

In this formula, \mathbf{H}_{fix} is then the field generated by a saturated outer part in the interior part. It can be obtained as

$-M_{SZ} - \mathbf{H}_{\text{var}}(h = 1)$, where \mathbf{H}_{var} is found from a saturated inner part ($h = 1$ for $r < r_N$). Finally, (2) is redefined as an integral between 0 and $r_N/\sqrt{A/K}$ with all terms unchanged except the dipolar part, for which the integrand becomes

$$\frac{-\mu_0 M_S}{2K_{\text{eff}}} [M_S + \mathbf{H}_{\text{dip}} \cdot \mathbf{m} + \mathbf{H}_{\text{fix}} \cdot (\mathbf{m} - \mathbf{z})]. \quad (\text{B6})$$

We note that the forward and backward Hankel transforms, plus mathematical operations required in Eqs. (9) and (11) to find the field of each layer acting on each layer, at each evolution step are extremely costly as compared to what is required for the four other field terms. As the Hankel transforms are multiplications of matrices, they can be factorized with the formulae of (9). Moreover, the dipolar field can be calculated by performing only once the determination of the factors inside ψ and deducing \mathbf{H}_{dip} for all layers in a last step. Very importantly, there is actually no need to repeat these operations at each evolution step. Because magnetostatic problems can be solved by superposition of simpler problems, as we have done with f and h , we can also do it for the source terms related to $\mathbf{m}(r)$ at each r . Given a sampling of r points r_1, r_2, \dots, r_N , we will precompute four dipolar field kernels $K_{h,f}^{r,z}$ for the dipolar fields due to f and h distributions, along r and z . They are $L \times L \times N \times N$ arrays where $K_{h,f}^{r,z}(j, i, r_j, r_i)$ store the magnetic fields in layer j at point r_j due to a unit (surface or volume) charge located in layer i at point r_i . By superposition of each elementary source, we find that the fields in each layer j are

$$\begin{bmatrix} H_{\text{dip}}^{r,z}(r_1) \\ H_{\text{dip}}^{r,z}(r_2) \\ \vdots \\ H_{\text{dip}}^{r,z}(r_N) \end{bmatrix} = \sum_{i=1}^L K_f^{r,z}(j, i, r_1 \dots r_N, r_1 \dots r_N) \begin{bmatrix} f_i(r_1) \\ f_i(r_2) \\ \vdots \\ f_i(r_N) \end{bmatrix} + \sum_{i=1}^L K_h^{r,z}(j, i, r_1 \dots r_N, r_1 \dots r_N) \begin{bmatrix} h_i(r_1) \\ h_i(r_2) \\ \vdots \\ h_i(r_N) \end{bmatrix}, \quad (\text{B7})$$

which gives self-interacting or interaction between two layers \mathbf{H}_{dip} in four matrix multiplications. Because there is no cost of having a fine sampling of k points once the kernels are computed, we make the choice of using a regular spacing of r points in order to get easier computation of other fields, and comparison with Mumax³, at the cost of some more initialization time.

Finally, we have chosen above a Cartesian description of $\mathbf{m} = (m_r, m_\phi, m_z)$. As the magnetization \mathbf{m} is normalized and evolves on the unit sphere, a description in spherical coordinates $\mathbf{m} = [\sin(\theta) \cos(\phi), \sin(\theta) \sin(\phi), \cos(\theta)]$, with θ polar and ϕ azimuthal angles, can be convenient

and is often used for describing the profile of magnetic skyrmions. We provide in [Appendix C](#) the expression of all fields and evolution step within spherical coordinates. Using it for the determination of the profiles is nevertheless not extremely suitable, as there is a definition issue for the azimuthal angle ϕ around $\mathbf{m} = \pm\mathbf{z}$, which degrades the convergence of the solver, and an additional computational complexity of involving multiple cos and sin functions. Because of these issues, we always use, in the present work, Cartesian coordinates for computing evolution steps (and maintain a unit magnetization everywhere), even if it may be convenient to display the final results with polar representation.

APPENDIX C: FIELDS WITH \mathbf{M} IN SPHERICAL COORDINATES

Effective fields associated to exchange, DMI and anisotropy

$$H_A = \frac{2A}{\mu_0 M_S} \begin{bmatrix} \frac{d^2\theta}{dr^2} \cos\theta \cos\phi - \frac{d^2\phi}{dr^2} \sin\theta \sin\phi \\ - \left(\frac{d\theta}{dr}\right)^2 \sin\theta \cos\phi - \left(\frac{d\phi}{dr}\right)^2 \sin\theta \cos\phi \\ - 2\frac{d\theta}{dr} \frac{d\phi}{dr} \cos\theta \sin\phi + \frac{1}{r} \frac{d\theta}{dr} \cos\theta \cos\phi \\ - \frac{1}{r} \frac{d\phi}{dr} \sin\theta \sin\phi - \frac{\sin\theta \cos\phi}{r^2} \\ \frac{d^2\theta}{dr^2} \cos\theta \sin\phi + \frac{d^2\phi}{dr^2} \sin\theta \cos\phi \\ - \left(\frac{d\theta}{dr}\right)^2 \sin\theta \sin\phi - \left(\frac{d\phi}{dr}\right)^2 \sin\theta \sin\phi \\ + 2\frac{d\theta}{dr} \frac{d\phi}{dr} \cos\theta \cos\phi + \frac{1}{r} \frac{d\theta}{dr} \cos\theta \sin\phi \\ + \frac{1}{r} \frac{d\phi}{dr} \sin\theta \cos\phi - \frac{\sin\theta \sin\phi}{r^2} \\ - \frac{d^2\theta}{dr^2} \sin\theta - \left(\frac{d\theta}{dr}\right)^2 \cos\theta - \frac{1}{r} \frac{d\theta}{dr} \sin\theta \end{bmatrix}, \quad (C1)$$

$$H_D = \frac{-2D}{\mu_0 M_S} \begin{bmatrix} \sin\theta \frac{d\theta}{dr} \\ 0 \\ \frac{d\theta}{dr} \cos\theta \cos\phi - \frac{d\phi}{dr} \sin\theta \sin\phi + \frac{\sin\theta \cos\phi}{r} \end{bmatrix}, \quad (C2)$$

$$H_K = \frac{2K_u}{\mu_0 M_S} \cos\theta \mathbf{z}. \quad (C3)$$

Integrands of (1) associated to exchange, DMI, and anisotropy energies

$$E_A = A \left[\left(\frac{d\theta}{dr}\right)^2 + \left(\frac{d\phi}{dr}\right)^2 \sin^2\theta + \frac{\sin^2\theta}{r^2} \right],$$

$$E_D = D \left[\frac{d\theta}{dr} \cos\phi - \frac{d\phi}{dr} \cos\theta \sin\theta \sin\phi + \frac{\cos\theta \sin\theta \cos\phi}{r} \right],$$

$$E_K = K_u \sin^2\theta. \quad (C4)$$

Magnetic charges for the determination of the dipolar field

$$f = M_S \left(\frac{d\theta}{dr} \cos\theta \cos\phi - \frac{d\phi}{dr} \sin\theta \sin\phi + \frac{\sin\theta \cos\phi}{r} \right),$$

$$h = -M_S \cos\theta. \quad (C5)$$

Evolution steps for (θ, ϕ)

$$\delta_\theta = \lambda (H_r \cos\theta \cos\phi + H_\phi \cos\theta \sin\phi + H_z \sin\theta),$$

$$\delta_\phi = \frac{\lambda}{\sin\theta} (H_\phi \cos\phi - H_r \sin\phi). \quad (C6)$$

APPENDIX D: ENERGY OF THE DOMAIN PROFILE IN CARTESIAN COORDINATES

We define here the Cartesian profile of a double domain wall with $m_x(\pm x) = \pm m_r(r)$, $m_y(\pm x) = m_\phi(r)$ and $m_z(\pm x) = m_z(r)$. The energies associated to symmetric exchange interaction, DMI, anisotropy, Zeeman fields are straightforward, while the dipolar field is found as in [Sec. II B](#), using the usual Fourier transform instead of the Hankel transform, with $h(x) = -M_S m_z(x)$ and $f(x) = M_S \partial m_x(x) / \partial x$. In the k space, all expressions are unchanged. We get, now using $\chi = x / \sqrt{A/K}$,

$$E_{\text{st}} = t\sqrt{AK_{\text{eff}}} \int_{-\infty}^{\infty} \left\{ \left(\frac{dm_x}{d\chi}\right)^2 + \left(\frac{dm_y}{d\chi}\right)^2 + \left(\frac{dm_z}{d\chi}\right)^2 + \frac{4D}{\pi D_c} \left(m_z \frac{dm_x}{d\chi} - m_x \frac{dm_z}{d\chi}\right) + \frac{K_u}{K_{\text{eff}}} (1 - m_z^2) + \frac{\mu_0 H_{\text{ext}} M_S}{K_{\text{eff}}} (1 - m_z) - \frac{\mu_0 M_S^2}{2K_{\text{eff}}} \left(1 + \frac{\mathbf{H}_{\text{dip}} \cdot \mathbf{m}}{M_S}\right) \right\} d\chi. \quad (D1)$$

APPENDIX E: DERIVATION OF THE VECTORS COMPOSING THE THIELE EQUATION

For a magnetization vector $\mathbf{m}(x, y)$ inside the structure we define $r = \sqrt{x^2 + y^2}$ and φ so that $x = r \cos\varphi$ and $y = r \sin\varphi$ (see [Fig. 1](#)). We then get

$$\mathbf{m} = \begin{bmatrix} m_r(r) \cos\varphi - m_\phi(r) \sin\varphi \\ m_\phi(r) \cos\varphi + m_r(r) \sin\varphi \\ m_z \end{bmatrix}, \quad (E1)$$

$$\frac{\partial \mathbf{m}}{\partial x} = \begin{bmatrix} \cos^2 \varphi \frac{\partial m_r}{\partial r} + \sin^2 \varphi \frac{m_r}{r} \\ -\sin \varphi \cos \varphi \frac{\partial m_\varphi}{\partial r} + \sin \varphi \cos \varphi \frac{m_\varphi}{r} \\ \cos^2 \varphi \frac{\partial m_\varphi}{\partial r} + \sin^2 \varphi \frac{m_\varphi}{r} \\ -\sin \varphi \cos \varphi \frac{\partial m_r}{\partial r} + \sin \varphi \cos \varphi \frac{m_r}{r} \\ \cos \varphi m_z \end{bmatrix}, \quad (\text{E2})$$

and

$$\frac{\partial \mathbf{m}}{\partial y} = \begin{bmatrix} \sin \varphi \cos \varphi \frac{\partial m_r}{\partial r} - \sin \varphi \cos \varphi \frac{m_r}{r} \\ -\sin^2 \varphi \frac{\partial m_\varphi}{\partial r} - \cos^2 \varphi \frac{m_\varphi}{r} \\ \sin \varphi \cos \varphi \frac{\partial m_\varphi}{\partial r} - \sin \varphi \cos \varphi \frac{m_\varphi}{r} \\ +\sin^2 \varphi \frac{\partial m_r}{\partial r} + \cos^2 \varphi \frac{m_r}{r} \\ \sin \varphi m_z \end{bmatrix}, \quad (\text{E3})$$

which gives

$$\left(\frac{\partial \mathbf{m}}{\partial x} \times \frac{\partial \mathbf{m}}{\partial y} \right) = \begin{bmatrix} -\frac{m_x}{r} \frac{\partial m_z}{\partial r} \\ -\frac{m_y}{r} \frac{\partial m_z}{\partial r} \\ -\frac{m_z}{r} \frac{\partial m_z}{\partial r} \end{bmatrix} \quad (\text{E4})$$

and then

$$\begin{aligned} \mathbf{G} &= -\frac{M_{StFM}}{\gamma} \int_{r=0}^{\infty} \int_{\varphi=0}^{2\pi} \left(-\frac{1}{r} \frac{\partial m_z}{\partial r} \right) r dr \\ &= \frac{2\pi M_{StFM}}{\gamma} [m_z(\infty) - m_z(0)]. \end{aligned} \quad (\text{E5})$$

By keeping only even orders both in $\cos \varphi$ and $\sin \varphi$ (others will integrate to zero), we get

$$\frac{\partial \mathbf{m}}{\partial x} \cdot \frac{\partial \mathbf{m}}{\partial y} = (\sin^2 \varphi - \cos^2 \varphi) \left(\frac{\partial m_r}{\partial r} \frac{m_\varphi}{r} - \frac{\partial m_\varphi}{\partial r} \frac{m_r}{r} \right) \quad (\text{E6})$$

and

$$\begin{aligned} \frac{\partial \mathbf{m}}{\partial x} \cdot \frac{\partial \mathbf{m}}{\partial x} &= \cos^2 \varphi \left[\left(\frac{\partial m_r}{\partial r} \right)^2 + \left(\frac{\partial m_\varphi}{\partial r} \right)^2 + \left(\frac{\partial m_z}{\partial r} \right)^2 \right] \\ &+ \sin^2 \varphi \left(\frac{1 - m_z}{r^2} \right), \end{aligned} \quad (\text{E7})$$

and we have a similar result with $\partial \mathbf{m} / \partial y \cdot \partial \mathbf{m} / \partial y$ so that after integration over φ we obtain

$$\begin{aligned} \mathcal{D}_{xx,yy} &= \frac{\pi M_{StFM}}{\gamma} \int_{r=0}^{\infty} \frac{1 - m_z^2}{r} + r \sum_{i=x,\varphi,z} \left(\frac{\partial m_i}{\partial r} \right)^2 dr, \\ \mathcal{D}_{xy,yx} &= 0. \end{aligned} \quad (\text{E8})$$

The torque exerted by the vertical spin current, polarized along y , considering only the dampinglike term originating

in the spin Hall effect of an in-plane current density J , is given by

$$\Gamma_{\text{SOT}} = \frac{\gamma \hbar}{2e\mu_0 M_{StFM}} (-\theta_{\text{SH}} J) \mathbf{m} \times (\mathbf{m} \times \mathbf{y}), \quad (\text{E9})$$

with θ_{SH} the effective spin Hall angle of the nearby materials enclosing the ferromagnetic layer. Inserting Γ_{SOT} into (15) we find after integration over φ

$$\begin{aligned} F_x &= -\theta_{\text{SH}} J \frac{\pi \hbar}{2e} \int_{r=0}^{\infty} r \left(\frac{\partial m_r}{\partial r} m_z - \frac{\partial m_z}{\partial r} m_r \right) + m_r m_z dr, \\ F_y &= \theta_{\text{SH}} J \frac{\pi \hbar}{2e} \int_{r=0}^{\infty} r \left(\frac{\partial m_\varphi}{\partial r} m_z - \frac{\partial m_z}{\partial r} m_\varphi \right) + m_\varphi m_z dr. \end{aligned} \quad (\text{E10})$$

-
- [1] I. Dzyaloshinsky, A thermodynamic theory of “weak” ferromagnetism of antiferromagnetics, *J. Phys. Chem. Solids* **4**, 241 (1958).
 - [2] T. Moriya, Anisotropic superexchange interaction and weak ferromagnetism, *Phys. Rev.* **120**, 91 (1960).
 - [3] M. Bode, M. Heide, K. von Bergmann, P. Ferriani, S. Heinze, G. Bihlmayer, A. Kubetzka, O. Pietzsch, S. Blügel, and R. Wiesendanger, Chiral magnetic order at surfaces driven by inversion asymmetry, *Nature* **447**, 190 (2007).
 - [4] M. Heide, G. Bihlmayer, and S. Blügel, Dzyaloshinskii-Moriya interaction accounting for the orientation of magnetic domains in ultrathin films: Fe/W(110), *Phys. Rev. B* **78**, 140403 (2008).
 - [5] A. N. Bogdanov and U. K. Röbber, Chiral Symmetry Breaking in Magnetic Thin Films and Multilayers, *Phys. Rev. Lett.* **87**, 037203 (2001).
 - [6] U. K. Röbber, A. N. Bogdanov, and C. Pfleiderer, Spontaneous skyrmion ground states in magnetic metals, *Nature* **442**, 797 (2006).
 - [7] G. Chen, A. Mascaraque, A. T. N’Diaye, and A. K. Schmid, Room temperature skyrmion ground state stabilized through interlayer exchange coupling, *Appl. Phys. Lett.* **106**, 242404 (2015).
 - [8] C. Moreau-Luchaire, C. Moutafis, N. Reyren, J. Sampaio, C. A. F. Vaz, N. Van Horne, K. Bouzehouane, K. Garcia, C. Deranlot, P. Warnicke, P. Wohlhüter, J.-M. George, M. Weigand, J. Raabe, V. Cros, and A. Fert, Additive interfacial chiral interaction in multilayers for stabilization of small individual skyrmions at room temperature, *Nat. Nanotech.* **11**, 444 (2016).
 - [9] S. Woo, K. Litzius, B. Krüger, M.-Y. Im, L. Caretta, K. Richter, M. Mann, A. Krone, R. M. Reeve, M. Weigand, P. Agrawal, I. Lemesh, M.-A. Mawass, P. Fischer, M. Kläui, and G. S. D. Beach, Observation of room-temperature magnetic skyrmions and their current-driven dynamics in ultrathin metallic ferromagnets, *Nat. Mater.* **15**, 501 (2016).
 - [10] S. Mühlbauer, B. Binz, F. Jonietz, C. Pfleiderer, A. Rosch, A. Neubauer, R. Georgii, and P. Böni, Skyrmion lattice in a chiral magnet, *Science* **323**, 915 (2009).

- [11] X. Z. Yu, Y. Onose, N. Kanazawa, J. H. Park, J. H. Han, Y. Matsui, N. Nagaosa, and Y. Tokura, Real-space observation of a two-dimensional skyrmion crystal, *Nature* **465**, 901 (2010).
- [12] J. Sampaio, V. Cros, S. Rohart, A. Thiaville, and A. Fert, Nucleation, stability and current-induced motion of isolated magnetic skyrmions in nanostructures, *Nat. Nanotech.* **8**, 839 (2013).
- [13] N. Nagaosa and Y. Tokura, Topological properties and dynamics of magnetic skyrmions, *Nat. Nanotech.* **8**, 899 (2013).
- [14] G. Yu, P. Upadhyaya, X. Li, W. Li, S. K. Kim, Y. Fan, K. L. Wong, Y. Tserkovnyak, P. K. Amiri, and K. L. Wang, Room-temperature creation and spin-orbit torque manipulation of skyrmions in thin films with engineered asymmetry, *Nano Lett.* **16**, 1981 (2016).
- [15] W. Jiang, X. Zhang, G. Yu, W. Zhang, X. Wang, M. Benjamin Jungfleisch, J. E. Pearson, X. Cheng, O. Heinonen, K. L. Wang, Y. Zhou, A. Hoffmann, and S. G. E. te Velthuis, Direct observation of the skyrmion Hall effect, *Nat. Phys.* **13**, 162 (2017).
- [16] K. Litzius, I. Lemesch, B. Krüger, P. Bassirian, L. Caretta, K. Richter, F. Büttner, K. Sato, O. A. Tretiakov, J. Förster, R. M. Reeve, M. Weigand, I. Bykova, H. Stoll, G. Schütz, G. S. D. Beach, and M. Kläui, Skyrmion Hall effect revealed by direct time-resolved X-ray microscopy, *Nat. Phys.* **13**, 170 (2017).
- [17] A. Neubauer, C. Pfleiderer, B. Binz, A. Rosch, R. Ritz, P. G. Niklowitz, and P. Böni, Topological Hall Effect in the *A* Phase of MnSi, *Phys. Rev. Lett.* **102**, 186602 (2009).
- [18] N. Kanazawa, Y. Onose, T. Arima, D. Okuyama, K. Ohoyama, S. Wakimoto, K. Kakurai, S. Ishiwata, and Y. Tokura, Large Topological Hall Effect in a Short-period Helimagnet MnGe, *Phys. Rev. Lett.* **106**, 156603 (2011).
- [19] A. Fert, N. Reyren, and V. Cros, Magnetic skyrmions: Advances in physics and potential applications, *Nat. Rev. Mat.* **2**, 17031 (2017).
- [20] D. Prychynenko, M. Sitte, K. Litzius, B. Krüger, G. Bourianoff, M. Kläui, J. Sinova, and K. Everschor-Sitte, Magnetic Skyrmion as a Nonlinear Resistive Element: A Potential Building Block for Reservoir Computing, *Phys. Rev. Appl.* **9**, 014034 (2018).
- [21] J. Zázvorka, F. Jakobs, D. Heinze, N. Keil, S. Kromin, S. Jaiswal, K. Litzius, G. Jakob, P. Virnau, D. Pinna, K. Everschor-Sitte, A. Donges, U. Nowak, and M. Kläui, Thermal skyrmion diffusion applied in probabilistic computing, [arXiv:1805.05924](https://arxiv.org/abs/1805.05924).
- [22] Y. Dovzhenko, F. Casola, S. Schlotter, T. X. Zhou, F. Büttner, R. L. Walsworth, G. S. D. Beach, and A. Yacoby, Magnetostatic twists in room-temperature skyrmions explored by nitrogen-vacancy center spin texture reconstruction, *Nat. Commun.* **9**, 2712 (2018).
- [23] S. A. Montoya, S. Couture, J. J. Chess, J. C. T. Lee, N. Kent, D. Henze, S. K. Sinha, M.-Y. Im, S. D. Kevan, P. Fischer, B. J. McMorran, V. Lomakin, S. Roy, and E. E. Fullerton, Tailoring magnetic energies to form dipole skyrmions and skyrmion lattices, *Phys. Rev. B* **95**, 024415 (2017).
- [24] W. Legrand, J.-Y. Chauleau, D. Maccariello, N. Reyren, S. Collin, K. Bouzehouane, N. Jaouen, V. Cros, and A. Fert, Hybrid chiral domain walls and skyrmions in magnetic multilayers, *Sci. Adv.* **4**, eaat0415 (2018).
- [25] N. Romming, C. Hanneken, M. Menzel, J. E. Bickel, B. Wolter, K. von Bergmann, A. Kubetzka, and R. Wiesendanger, Writing and deleting single magnetic skyrmions, *Science* **341**, 636 (2013).
- [26] N. Romming, A. Kubetzka, C. Hanneken, K. von Bergmann, and R. Wiesendanger, Field-dependent Size and Shape of Single Magnetic Skyrmions, *Phys. Rev. Lett.* **114**, 177203 (2015).
- [27] W. Jiang, P. Upadhyaya, W. Zhang, G. Yu, M. B. Jungfleisch, F. Y. Fradin, J. E. Pearson, Y. Tserkovnyak, K. L. Wang, O. Heinonen, S. G. E. te Velthuis, and A. Hoffmann, Blowing magnetic skyrmion bubbles, *Science* **349**, 283 (2015).
- [28] O. Boulle, J. Vogel, H. Yang, S. Pizzini, D. de Souza Chaves, A. Locatelli, T. O. Mentès, A. Sala, L. D. Buda-Prejbeanu, O. Klein, M. Belmeguenai, Y. Roussigné, A. Stashkevich, S.-M. Chérif, L. Aballe, M. Foerster, M. Chshiev, S. Auffret, I. M. Miron, and G. Gaudin, Room-temperature chiral magnetic skyrmions in ultrathin magnetic nanostructures, *Nat. Nanotech.* **11**, 449 (2016).
- [29] M. He, G. Li, Z. Zhu, Y. Zhang, L. Peng, R. Li, J. Li, H. Wei, T. Zhao, X.-G. Zhang, S. Wang, S.-Z. Lin, L. Gu, G. Yu, J. W. Cai, and B.-G. Shen, Evolution of topological skyrmions across the spin reorientation transition in Pt/Co/Ta multilayers, *Phys. Rev. B* **97**, 174419 (2018).
- [30] A. Bernand-Mantel, L. Camosi, A. Wartelle, N. Rougemaille, M. Darques, and L. Ranno, The skyrmion-bubble transition in a ferromagnetic thin film, *Sci. Post Phys.* **4**, 27 (2018).
- [31] A. Hrabec, J. Sampaio, M. Belmeguenai, I. Gross, R. Weil, S. M. Chérif, A. Stashkevich, V. Jacques, A. Thiaville, and S. Rohart, Current-induced skyrmion generation and dynamics in symmetric bilayers, *Nat. Commun.* **8**, 15765 (2017).
- [32] R. Tolley, S. A. Montoya, and E. E. Fullerton, Room-temperature observation and current control of skyrmions in Pt/Co/Os/Pt thin films, *Phys. Rev. Mater.* **2**, 044404 (2018).
- [33] A. Soumyanarayanan, M. Raju, A. L. G. Oyarce, A. K. C. Tan, M.-Y. Im, A. P. Petrović, P. Ho, K. H. Khoo, M. Tran, C. K. Gan, F. Ernult, and C. Panagopoulos, Tunable room-temperature magnetic skyrmions in Ir/Fe/Co/Pt multilayers, *Nat. Mater.* **16**, 898 (2017).
- [34] W. Legrand, D. Maccariello, N. Reyren, K. Garcia, C. Moutafis, C. Moreau-Luchaire, S. Collin, K. Bouzehouane, V. Cros, and A. Fert, Room-temperature current-induced generation and motion of sub-100 nm skyrmions, *Nano Lett.* **17**, 2703 (2017).
- [35] I. Lemesch, F. Büttner, and G. S. D. Beach, Accurate model of the stripe domain phase of perpendicularly magnetized multilayers, *Phys. Rev. B* **95**, 174423 (2017).
- [36] F. Büttner, I. Lemesch, and G. S. D. Beach, Theory of isolated magnetic skyrmions: From fundamentals to room temperature applications, *Sci. Rep.* **8**, 4464 (2018).
- [37] S. Woo, K. M. Song, H.-S. Han, M.-S. Jung, M.-Y. Im, K.-S. Lee, K. S. Song, P. Fischer, J.-I. Hong, J. W. Choi, B.-C. Min, H. C. Koo, and J. Chang, Spin-orbit torque-driven skyrmion dynamics revealed by time-resolved X-ray microscopy, *Nat. Commun.* **8**, 15573 (2017).

- [38] Y.-O. Tu, Determination of magnetization of micromagnetic wall in bubble domains by direct minimization, *J. Appl. Phys.* **42**, 5704 (1971).
- [39] W. J. DeBonte, Properties of thick-walled cylindrical magnetic domains in uniaxial platelets, *J. Appl. Phys.* **44**, 1793 (1973).
- [40] R. Tomasello, K. Y. Guslienko, M. Ricci, A. Giordano, J. Barker, M. Carpentieri, O. Chubykalo-Fesenko, and G. Finocchio, Origin of temperature and field dependence of magnetic skyrmion size in ultrathin nanodots, *Phys. Rev. B* **97**, 060402 (2018).
- [41] A. O. Leonov, T. L. Monchesky, N. Romming, A. Kubetzka, A. N. Bogdanov, and R. Wiesendanger, The properties of isolated chiral skyrmions in thin magnetic films, *New J. Phys.* **18**, 065003 (2016).
- [42] M. E. Knoester, J. Sinova, and R. A. Duine, Phenomenology of current-skyrmion interactions in thin films with perpendicular magnetic anisotropy, *Phys. Rev. B* **89**, 064425 (2014).
- [43] S. Rohart and A. Thiaville, Skyrmion confinement in ultrathin film nanostructures in the presence of Dzyaloshinskii-Moriya interaction, *Phys. Rev. B* **88**, 184422 (2013).
- [44] A. Vansteenkiste, J. Leliaert, M. Dvornik, M. Helsen, F. Garcia-Sanchez, and B. Van Waeyenberge, The design and verification of MuMax3, *AIP Adv.* **4**, 107133 (2014).
- [45] A. Bogdanov and A. Hubert, The properties of isolated magnetic vortices, *Phys. Stat. Sol. B* **186**, 527 (1994).
- [46] S. Rohart, J. Miltat, and A. Thiaville, Path to collapse for an isolated Néel skyrmion, *Phys. Rev. B* **93**, 214412 (2016).
- [47] S. von Malottki, B. Dupé, P. F. Bessarab, A. Delin, and S. Heinze, Enhanced skyrmion stability due to exchange frustration, *Sci. Rep.* **7**, 12299 (2017).
- [48] P. F. Bessarab, G. P. Müller, I. S. Lobanov, F. N. Rybakov, N. S. Kiselev, H. Jónsson, V. M. Uzdin, S. Blügel, L. Bergqvist, and A. Delin, Lifetime of racetrack skyrmions, *Sci. Rep.* **8**, 3433 (2018).
- [49] A. Thiaville, S. Rohart, E. Jué, V. Cros, and A. Fert, Dynamics of Dzyaloshinskii domain walls in ultrathin magnetic films, *Europhys. Lett.* **100**, 57002 (2012).
- [50] J. Iwasaki, M. Mochizuki, and N. Nagaosa, Current-induced skyrmion dynamics in constricted geometries, *Nat. Nanotech.* **8**, 742 (2013).
- [51] J. Iwasaki, M. Mochizuki, and N. Nagaosa, Universal current-velocity relation of skyrmion motion in chiral magnets, *Nat. Commun.* **4**, 1463 (2013).
- [52] M.-W. Yoo, V. Cros, and J.-V. Kim, Current-driven skyrmion expulsion from magnetic nanostrips, *Phys. Rev. B* **95**, 184423 (2017).
- [53] K.-W. Kim, K.-W. Moon, N. Kerber, J. Nothhelfer, and K. Everschor-Sitte, Asymmetric skyrmion Hall effect in systems with a hybrid Dzyaloshinskii-Moriya interaction, *Phys. Rev. B* **97**, 224427 (2018).
- [54] X. Zhang, Y. Zhou, and M. Ezawa, Magnetic bilayer-skyrmions without skyrmion Hall effect, *Nat. Commun.* **7**, 10293 (2016).
- [55] C. Hanneken, F. Otte, A. Kubetzka, B. Dupé, N. Romming, K. von Bergmann, R. Wiesendanger, and S. Heinze, Electrical detection of magnetic skyrmions by tunnelling non-collinear magnetoresistance, *Nat. Nanotech.* **10**, 1039 (2015).
- [56] D. M. Crum, M. Bouhassoune, J. Bouaziz, B. Schweglinghaus, S. Blügel, and S. Lounis, Perpendicular reading of single confined magnetic skyrmions, *Nat. Commun.* **6**, 8541 (2015).
- [57] D. Maccariello, W. Legrand, N. Reyren, K. Garcia, K. Bouzehouane, S. Collin, V. Cros, and A. Fert, Electrical detection of single magnetic skyrmions in metallic multilayers at room temperature, *Nat. Nanotechnol.* **13**, 233 (2018).
- [58] I. Lemesch and G. S. D. Beach, Twisted domain walls and skyrmions in perpendicularly magnetized multilayers, *Phys. Rev. B* **98**, 104402 (2018).
- [59] H. Johnson, An improved method for computing a discrete Hankel transform, *Comp. Phys. Comm.* **43**, 181 (1987).